

1 **Fifty-year seasonal variability of East African droughts and floods recorded in Central**
2 **Afar lake sediments (Ethiopia) and their connections with ENSO**

3
4 Carlo Mologni ^{1*}, Marie Revel ¹, Eric Chaumillon ², Emmanuel Malet ³, Thibault Coulombier
5 ², Pierre Sabatier ³, Pierre Brigode ¹, Gwenael Hervé ⁴, Anne-Lise Develle ³, Laure Schenini ¹,
6 Medhi Messous ¹, Gourguen Davtian ⁶, Alain Carré, ⁶, Delphine Bosch ⁷, Natacha Volto ²,
7 Clément Ménard ⁵, Lamya Khalidi ⁶, Fabien Arnaud ³

8
9 ¹ Université Côte d'Azur, CNRS, OCA, IRD, Geoazur, 250 rue Albert Einstein, 06500 Valbonne,
10 France.

11 ² University of La Rochelle, UMR CNRS 7266 LIENSs, La Rochelle, France.

12 ³ Environnement Dynamique et Territoire de Montagne (EDYTEM), CNRS, Université Savoie Mont-
13 Blanc, Le Bourget du lac, France.

14 ⁴ Laboratoire des Sciences du Climat et de l'Environnement/IPSL, CEA, CNRS, UVSQ, University of
15 Paris-Saclay, Gif-sur-Yvette, France.

16 ⁵ EPCC, Centre Européen de Préhistoire, Avenue Léon-Jean Grégory - 66720 – Tautavel, France

17 ⁶ Université Côte d'Azur, CNRS, CEPAM – UMR 7264, 24 av. des Diables Bleus 06300 Nice, France.

18 ⁷ Géosciences Montpellier, UMR-CNRS 5243, Université de Montpellier, 34095 Montpellier, France

19 *Corresponding author

20
21 **Abstract**

22 Understanding past and present hydro-system feedbacks to global ocean-atmospheric interactions
23 represents one of the main challenges to preventing droughts, extreme events and related human
24 catastrophes in the face of global warming, especially in arid and semiarid environments. In eastern
25 Africa, the El Niño-Southern Oscillation (ENSO) was identified as one of the primary drivers of
26 precipitation variability affecting water availability. However, the northern East African Rift System
27 (EARS) still suffers ~~from ENSO climate teleconnection and the~~ from the underrepresentation of
28 ~~predictive-~~ and ENSO teleconnection models because of the scarcity of local-to-regional historical or
29 palaeo-data.

30 In this paper, we provide a 50-year seasonal flood/drought chronicle of the Awash River catchment from
31 the study of laminated sediment from Gemeri and Afambo lakes (Central Afar region, Ethiopia), with
32 the aim of reconstructing the magnitude of regional hydro-climatic events. Pluri-centimetric micro-
33 laminated lithogenic facies alternating with pluri-millimetric carbonate-enriched facies are investigated
34 in both lakes. We couple dating methods including radiocarbon, short-lived radionuclides,
35 palaeomagnetic field variations and varve counting on both lake deposits to build a high-resolution age
36 model and to discuss the regional hydro-sedimentary dynamics of the Awash River over the last ~700
37 years, with a focus on the last fifty years.

38 Using a multiproxy approach, we observe that following a multi-centennial enhanced hydrological
39 period, the two lakes experienced a gradual decrease in river load inflow since 1979 CE, attaining
40 extreme drought and high evaporative conditions between 1991 and 1997 CE. In 2014, the construction
41 of a dam and the improvement of agricultural ~~hydraulic-water~~ management in the lower Awash River

42 plain impacted the ~~erodibility~~ of local soils and the hydro-sedimentary balance of the lake basins, as
43 evidenced by a disproportionate sediment accumulation rate.

44 Comparison of our quantitative reconstruction with i) lake water surface evolution ~~expressed in Km³~~,
45 ii) the interannual Awash River flow rates ~~expressed in mm/yr~~, and iii) the El Niño 3.4 model highlights
46 the intermittent connections between ENSO ~~SST~~ Sea Surface Temperature anomalies, regional droughts
47 and hydrological conditions in the northern EARS.

48 1 Introduction

49 According to the Sixth Assessment Report of the Intergovernmental Panel on Climate Change (IPCC),
50 climate warming has been more rapid in Africa in recent decades than in any other region of the world
51 (IPCC, 2022). Between March and August across Eastern Africa, the monsoonal rainy season is vital
52 for agricultural production and thus for national food security, especially in more susceptible areas such
53 as along the Rift Valley and over distal lowlands. During the last ~50 years, recurrent reduced rainy
54 seasons have had substantial environmental, humanitarian and economic impacts, including agriculture
55 and ecosystem sustainability (Palmer et al., 2023). Global climate projections further suggest that the
56 Horn of Africa will experience strong disturbances of its usual hydrological cycle, with both increasing
57 frequency of intense rainfall events leading to enhanced flash-flood hazards and a generalized scarcity
58 of rainfall, leading to frequent severe drought episodes (Palmer et al., 2023). Such climatic instability
59 may induce the collapse of the local food production system, leading to famine, as it occurred in the
60 decades between 1970 and 1990 (FAO, 2000). More recently, the shorter-than-normal 2021 rainy season
61 led to a 70% reduction in average precipitation compared with seasonal norms, which raised an
62 international alert and mobilization for the mitigation of desertification processes in the Horn of Africa
63 (FAO, 2022).

64 Facing such evidence, eastern Africa is currently the focus for understanding recent (Late Holocene
65 seale) past climate dynamics (Lennard et al., 2018) to simulate future projections, support regional
66 ecosystem sustainability (Niang et al., 2014) and reduce rural population vulnerability to climate
67 warming (FAO, 2022). Palaeoclimatic reconstructions have long been used to understand past climate
68 variability to build more robust future climatic models in Africa. Even if global climate and hydrological
69 model simulations have made considerable progress, reconstructions or tendencies of future
70 precipitation and atmospheric dynamics in eastern Africa ~~—source of moisture fluxes from the Atlantic~~
71 ~~or Indian Oceans (Marzin and Braconnot, 2009)~~— which affect continental hydrology at the regional-to-
72 local scale remain to be developed (Dosio et al., 2019; Lennard et al., 2018). Indeed, the lack of
73 widespread regional-to-local palaeoclimatic data makes it difficult to establish regional climatic models
74 and the link between global hydroclimate variability and the functioning of specific hydro-systems.

75 In East Africa, precipitation variability is influenced by multiple interactions between patterns of remote
76 climate forcing, regional circulation and local geographic factors acting at local and global scales
77 (Nicholson, 2017). At a wider scale, the El Niño-Southern Oscillation (ENSO) was identified as one of

78 the primary drivers of precipitation in eastern Africa (Ficchi et al., 2021; Nicholson, 2017; Palmer et al.,
79 2023). More research on regional and high-temporal resolution relationships between ENSO and
80 flood/drought impacts in the present and in the past is increasingly needed (Ficchi et al., 2021; Ward et
81 al., 2014). With the aim of filling this gap, this paper focuses on the acquisition of new hydro-
82 sedimentary datasets (i.e., decennial to seasonal scale resolution) thanks to the study of lacustrine
83 sedimentary sequences from one of the wider river catchments in the northern East African Rift System
84 (EARS), namely the Awash River basin (Fig. 1).

85 As flood occurrence and magnitude of the Awash River are mainly linked to fluctuation of the Ethiopian
86 Highland precipitation regime over time, the establishment of regional flood chronicles from natural
87 archives is key to evaluating the evolution of precipitation variability on land (Ficchi et al., 2021;
88 Mologni et al., 2020; Wilhelm et al., 2022). Of all of the natural archives for hydrological reconstruction,
89 lakes are privileged because they act as natural sinks, continuously trapping erosion products from an
90 entire catchment over a long period (Sabatier et al., 2022; Wilhelm et al., 2018). Indeed, during flood
91 events, water-transported detrital particles (or sediment discharge) are deposited on the lake bottom in
92 the form of graded layers that differ from the intra-lake sedimentation related to lake productivity. Thus,
93 lake sedimentary deposits are valuable to fully understand the relationships between hydroclimate,
94 rainfall, floods, droughts and lake water conditions at the regional scale.

95 This paper presents the results from a multiproxy study combining a seismic survey with
96 sedimentological and geochemical analyses performed on archives from the Afambo and Gemeri lakes
97 located in the Abhe lake basin (Central Afar Region, Ethiopia, Fig. 1). The main objective of this study
98 is to quantify variations of long-term Awash River solid sedimentary discharges to establish regional
99 flood activity chronicle and to reconstitute the hydrological regime of the Awash River. ~~Moreover,~~
100 ~~human activities can also play a key role in sediment availability, which is a function of soil erodibility~~
101 ~~and transport processes (Arnaud et al., 2016; Arnaud and Sabatier, 2022; Bajard et al., 2017, 2016;~~
102 ~~Syvitski et al., 2022).~~ We aim first to identify the hydro-sedimentary processes in the Afambo and
103 Gemeri Lake basins (Central Afar Region, Ethiopia) under human and hydroclimate/meteorological
104 forcing over the long-term. Finally, we compare these flood and drought chronicles with global ENSO
105 records and discuss the interaction between atmospheric anomalies, droughts and hydrological
106 conditions in the northern EARS.

107 2 Study site: hydrological and geomorphological settings

108 2.1 Regional hydroclimatic patterns

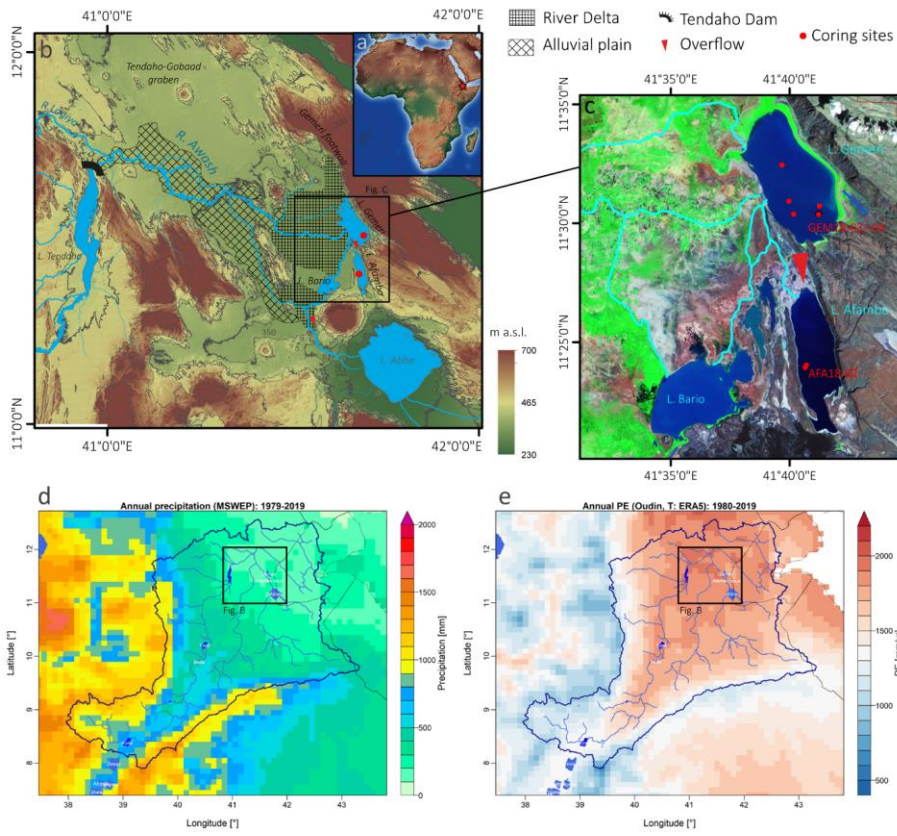
109 The Abhe Lake basin, located at the northern extremity of the EARS (~12° N), is the widest and longest
110 rifting-controlled sedimentary basin of the Afar Rift System (Fig. ~~1A1a~~). It corresponds to the
111 topographic depression of the lower Awash valley (Fig. ~~1B1b~~) consisting of an area of 6 000 km²
112 (Mologni et al., 2021). The Central Afar Region is currently a desert receiving ~400 mm/yr of local

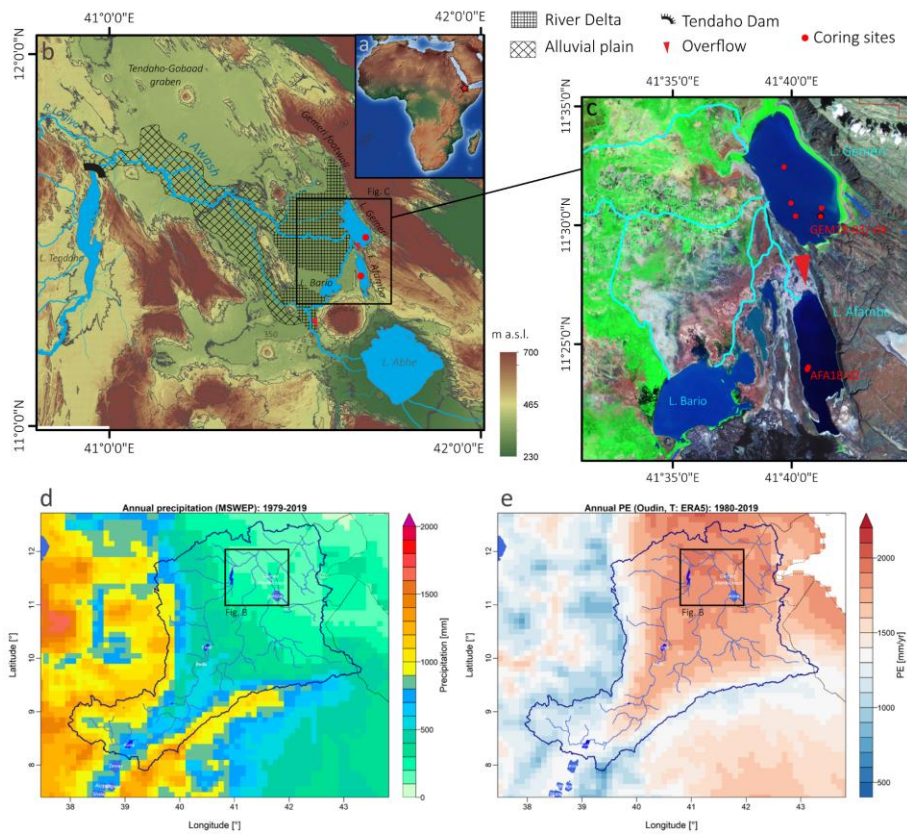
Code de champ modifié

Mis en forme : Couleur de police : Automatique, Anglais (Royaume-Uni)

Mis en forme : Couleur de police : Automatique, Anglais (Royaume-Uni)

113 precipitation (Fig. 4D1d) with a mean annual evapotranspiration of ~2000 mm/yr (Fig. 4E1e). In such
114 a dry context, the permanency of waterbodies such as lakes Gemberi and Afambo (Fig. 4E1e) is mainly
115 supported by their hydrological dependence on permanent Awash River water supplies originating in
116 the Ethiopian highlands (mean annual precipitation ~1000 mm/yr; Fig. 4D1d), whereby the hydrological
117 regime is dominated by seasonal rainfall pertaining to the southwest African monsoon. With a drainage
118 basin surface of over 112,700 km², the Awash River has an annual runoff of 4.6 BM³. However, 72%
119 of it is lost to evapotranspiration in the lowlands (Taddese et al., 2010).
120





122
 123 **Figure 1:** Geographical, geomorphological and hydrological contexts of the study area and coring sites. **A)** Location of the
 124 Central Afar Region on a topographic map of Africa (red star); **B)** DEM-Digital Elevation Model of the Lake Abhe basin
 125 (SRTM) corresponding to the Lower Awash Valley with the location of Gemeri, Afambo and Abhe waterbodies, the
 126 corresponding alluvial plain and the Awash River delta, the main coring sites (red dots), the overflow directions and the
 127 Tendaho dam; **C)** Focus on Lakes Afambo and Gemeri study sites with the location of coring sites (red dots), the local
 128 hydrographic network (light blue lines) and the overflow direction between the waterbodies; **D)** mean annual precipitation
 129 over the Awash River and Lake Abhe basins estimated over the 1979-2019 period using the MSWEP dataset Beck et al. (2019).
 130 **E)** Mean annual potential evapotranspiration over the Awash River and Lake Abhe basins estimated using the Oudin et al.
 131 (2005) formula and the air temperature of the ERA5 dataset Hersbach et al. (2020).

132 When it feeds into Lakes Gemeri and Afambo Lakes, the Awash River has only crossed recent
 133 geological formations subsequent to the formation of the Oligocene Ethiopian basaltic trap flows. The
 134 lower Awash Valley is mainly composed of stratoid basalts formed between 4 and 0.4 Ma (Awaleh et
 135 al., 2016, Barberi and Varet, 1977; Varet, 2018) and intra-graben Quaternary accumulations, which still
 136 belong mainly to the Stratoid series group.

137 2.2 Local geomorphological context

138 The northern part of the Lake Abhe basin is composed of an alluvial plain corresponding to irrigated
 139 agricultural fields and extended anthropogenic water channels, and a lobate delta in its lower part (Fig.

140 1b). The remaining edges of the basin are composed of desert plains and basaltic/rhyolitic outcrops that
141 constitute the Tendaho-Gobaad graben horsts (Fig. 1b). The delta fan spreads ~60 km from the northern
142 Gemeri footwall fault through the Gemeri and Bario waterbodies until the Dama Ale volcano slopes to
143 the south (Fig. 1b).

144 The Awash freshwater supplies first reach Lake Gemeri (11°51'N, 41°69' E), and overflowing into Lake
145 Afambo (11° 40' N, 41° 68' E). In contrast to Gemeri, Lake Afambo is not located on the delta fan and
146 does not possess any aerial estuary (Fig. 4B1b, 6c). Indeed, Afambo Lake is reached during the dry
147 season by a single water channel and is permanently separated from the deltaic swamps by north-south
148 basaltic outcrops (Fig. 1c, 2a). The rest of the Awash water supply is drained by the delta to the Bario
149 waterbody and to the terminal river channel that flows down to Lake Abhe (Fig. 4B1b, 6c).

150 The local hydrological network led us to select two complementary coring sites for this study: Lake
151 Gemeri, which borders the prodeltaic zone, mostly records the sedimentary signal from fluvial dynamics
152 (Awash River solid load), and Lake Afambo, which is partially disconnected from deltaic dynamics, has
153 the potential to record fine-grained sediment inputs, lacustrine primary productivity processes and to
154 preserve the sedimentary record from hiatuses due to deltaic erosional dynamics.

155 The hydrological network of the Lower Awash River plain has been modified by the building of a dam
156 for the agricultural development of this area conducted by the "*Tendaho Dam and Irrigation Project*"
157 (Dereje et al., 2018; Kidane et al., 2014). The dam is located upon entry of the Awash River waters into
158 the Lake Abhe basin area (Fig. 1b). The construction project began in 2010, and the dam started working
159 in early 2014. Such massive infrastructure has led to the formation of the Tendaho artificial lake (Fig.
160 1b) and the current network of irrigation channels in the alluvial plain.

161 **3 Materials and methods**

162 **3.1 Analysis of the water surface evolution of Lake Gemeri from satellite** 163 **images (1984 – 2019)**

164 We conducted imagery analyses of the water surfaces of Lakes Gemeri and Afambo from 1984 to 2021.
165 We used the "Global Surface Water" dataset from the Copernicus Programme, which was generated
166 using 4,716,475 **monthly and sub-monthly** scenes from Landsat 5, 7, and 8 acquired between March 1984
167 and December 2021 by Landsat satellites provided by the USGS and NASA. The dataset contains maps
168 of the location and temporal distribution of surface water from 1984 to 2021 at 30 m resolution and
169 provides statistics on the extent and change of those water surfaces. For more information, refer to the
170 associated journal article by Pekel et al. (2016). From this dataset, we computed statistics about the
171 extent and change of the water surfaces. Using Envi software, version 5.4, we created a Meta image
172 with the 37 water surface maps from 1985 to 2021 and generated statistics for the Meta image, which
173 were then exported.

174 However, for the years 1988, 1989, 1990, 1992, 1993, 1996, and 1997, the “Global Surface Water”
175 dataset algorithm failed to concretely calculate the water surfaces, resulting in imprecise or missing data.
176 As a result, we employed the quality assessment (QA) band in Landsat 5 images, which provides
177 information on features such as clouds, shadows, ice, bare land, and water. Classification
178 algorithms were applied to assign binary values to bits in the QA band based on pixel characteristics.
179 By importing archives from the USGS and utilizing the Pixel_QA band associated with the available
180 images, a water mask was created. This water mask allowed us to perform zonal statistics using ArcGIS
181 Pro 3.0.3.

182 **3.2 Seismic survey**

183 In December 2018, a seismic reflection survey was conducted in the southernmost part of Lake Gemberi
184 with the aim of exploring the internal architecture of the lake sedimentary fill and choosing the location
185 of the coring site. The acquisition of 12 seismic profiles of Lake Gemberi (Fig. S1, S2) was performed
186 using an IxBlue ECHOES 5000 CHIRP echo-sounder (LIENSs laboratory, La Rochelle, France). Chirp
187 frequency band 2000 - 8000 Hz was selected, with a chirp length of 50 ms. Chirp data processing
188 included auto grain control, time varying gain, staking of adjacent traces, and swell filtering.

189 **3.3 Coring of Gemberi and Afambo Lakes**

190 In December 2018, 10 short sedimentary cores were retrieved from Lakes Gemberi and Afambo during
191 the CLIMAFAR 2018 survey. Shorter cores were retrieved using a UWITEC gravity corer, while a
192 homemade modified Nesje-like corer permitted us to reach slightly more than 2 m sediment depth in
193 Lake Gemberi (Fig. 1c). Details about the coring operations can be found on the French National
194 Cybercatheque (<https://cybercarotheque.fr/index.php?ope=530>).

195 We focused the present study on cores collected in the deepest part of each lake, i.e., GEM18-03 (length
196 144 cm, IGSN number TOAE0000000354) and GEM18-04 (209 cm, IGSN number:
197 TOAE0000000356) taken at 6 m water depth in Lake Gemberi, and AFA18-02 (173 cm, IGSN number
198 TOAE0000000348) taken in Lake Afambo at 18 m water depth. GEM18-04 was cut into two parts in
199 the field, and only the deepest part (109-209 cm below lake floor) of the overlapping core GEM18-03,
200 was studied here. Core sections were split length-wise, photographed at high resolution, and described
201 and logged in detail using the Munsell colour chart at the EDYTEM sedimentary lab facility. The
202 identification of specific layers on the overlapping sections GEM18-03 and GEM18-04B together with
203 the comparison of XRF core scanner and magnetic susceptibility signals led us to propose a 2.2 m long
204 composite sediment sequence from Lake Gemberi, hereafter called GEM18-03/04.

205 **3.4 Analytical methods**

206 **3.4.1 XRF core scanner on soft sediments, ICP–MS measurements and clay** 207 **mineralogy**

208 To characterize the variation in major elements throughout cores GEM18-03/04 and AFA18-02, we
209 performed non-destructive X-ray fluorescence (XRF) geochemical analyses on an AVAATECH Core
210 Scanner at the EDYTEM laboratory (CNRS-Université de Savoie Mont-Blanc, France). The XRF
211 analyses were performed following a 1 mm sampling step for the AFA18-02 section A, 2 mm for the
212 lower section B (live time = 20s), and 5 mm for the GEM18-03/04 core. At each step, two successive
213 measurements were performed at 10 kV (0.12mA) and 30 kV (0.15mA) voltages to assess the
214 contribution of lighter (Al, Si, S, K, Ca, Ti, Mn, Fe) and heavier (Br, Sr, Rb, Zr, Pb) elements,
215 respectively. Each individual power spectrum was transformed by deconvolution into relative contents
216 of each computed element expressed in counts per second (cps). XRF data were subsequently
217 transformed with a Centred Log-Ratio transformation package on R© software, with the aim of
218 circumventing problems associated with matrix effects (e.g., variable water content and grain-size
219 distribution) and irregularities of the core surface (Weltje and Tjallingii, 2008).

220 Principal component analysis (PCA) was performed on the XRF results using R© software (Sup. Mat.
221 C) with the aim of characterizing the main geochemical signatures of particles composing the GEM18-
222 03/04 and AFA18-02 sediments.

223 Major and trace element analyses were performed with a Quadrupole ICP–MS (AETE-ISO platform,
224 Geosciences Montpellier, France) on 500 mg of powdered and homogenized sediment sample for 6
225 discrete samples in the GEM18-03/04 core and 11 discrete samples from the AFA18-02 core (Rauch et
226 al., 2006).

227 X-ray diffraction analyses on clay minerals were performed on 5 samples from the GEM18-03/-04
228 sequence at the LHyGS laboratory CNRS-UMR7517 (Strasbourg, France) (Sup. Mat. F). Sediments
229 were treated with HCl (10%) solution to avoid any carbonate content. Suspended clay fractions were
230 separated following the procedure in Jackson (2005) and mounted on thin sections for oriented clay
231 XRD analyses. With the aim of acquiring the whole diffraction spectrum, four diffractograms were
232 obtained using a D8-Advance-Eco machine from the same sample with normal treatment, ethylene-
233 glycol treatment, hydrazine treatment, and heat treatment for 4 h at 490°C. The semiquantitative content
234 of clay minerals (%) was obtained from MacDiff version 4.1.2 software as a 2 θ ° counts per second (cps)
235 spectrum area measurement.

236 **3.4.2 Sedimentological analyses**

237 Grain-size analyses were performed at the Geoazur laboratory using a Coulter-LS2000 with a size range
238 between 0.005 μm and 3775 μm . The analysis was performed following a 2.5 mm sampling step for the
239 AFA18-02 core. We determined the grain size of the intercepts for 10%, 50% and 90% of the cumulative
240 grain size curves (named ~~Q90-D90~~, ~~Q50-D50~~ and ~~Q10-D10~~ values; Folk and Ward, 1957). We use the

241 coarsest fraction (Q90D90) to characterize the deposit energy and to propose a hydrodynamic
242 interpretation as suggested by Wilhelm et al., (2018).

243 Optical microscopic analyses were focused on 8 thin sections (10 x 2 cm) sampled from the AFA18-02
244 sequence and processed at the litho-preparation facilities of the EDYTEM laboratory (Arnaud and
245 Sabatier, 2022). Microscopic observations were obtained on a Leica DM4 P at the Geoazur Laboratory
246 at 25x and 1000x magnification using plane-polarized (PPL), crossed-polarized (XPL) and oblique
247 incident (OIL) lights. Loss On Ignition (LOI) was performed on crushed sediment for each analysed
248 sample at the CEPAM-UMR7264 laboratory (Sup. Mat. E). Samples were heated for 24 h at 100°C
249 with the aim to determine the residual water and gypsum content. Subsequently samples were heated
250 for 4 h at 550°C with the aim to determine total content measures of organic carbon (Santisteban et al.,
251 2004). LOI is expressed in percentage (%).
252

253 3.4.3 Chronology of Gemer and Afambo Lake sequences

254 On the GEM18-03/04 sediment sequence, we combined short-lived radionuclides (^{210}Pb and ^{137}Cs), ^{14}C
255 measurements and palaeomagnetic analyses to build a reliable age-depth model along the 2.2 m of the
256 composite section. A continuous sampling step of 6 cm was applied over the uppermost 66 cm of
257 GEM18 to determine ^{210}Pb , ^{226}Ra and ^{137}Cs activities using well-type germanium detectors (SAGE
258 Well) located below 1700 m of rocks at the “laboratoire souterrain de Modane” (CNRS-Université
259 Grenoble Alpes) to reduce the influence of cosmic rays on gamma measurements (Reyss et al., 1995).
260 Radionuclide-based age models were computed using the *serac* R package (Bruel and Sabatier, 2020).
261 For the ^{210}Pb ex model, we choose the CFCS (Constant Flux Constant Sedimentation) model because
262 CRS (Constant Rate of Supply) cannot be applied in this context in regard to 1/ the hiatus (which affect
263 the ^{210}Pb ex inventory) and 2/ the age of the AFA core which not allow to estimate the total ^{210}Pb ex
264 inventory need for CRS model calculation. We not applied the CIC (Constant Initial Concentration)
265 model because it will result in age inversion in regard to ^{210}Pb ex fluctuation.

266 ^{14}C measurements were performed on 9 bulk organic matter and 4 shell samples (Sup. Mat. I, Fig. S23)
267 using the ARTEMIS accelerator mass spectrometry (AMS) facility at the LSCE-LMC14 laboratory
268 (Gif-sur-Yvette, France).

269 Palaeomagnetic measurements were performed on the entirety of the GEM18-03/-04 composite section.
270 The principle of the palaeomagnetic method is to compare the declination, inclination and relative
271 palaeointensity (RPI) records from the dated core with a reference curve of the secular variations in the
272 geomagnetic field (Crouzet et al., 2019; Haberzettl et al., 2019; Li et al., 2021; Ólafsdóttir et al., 2013).
273 Measurements were performed at the LSCE on u-channels sampled from the center of the GEM18-03
274 and GEM18-04B half cores. The direction of the characteristic remnant magnetization (ChRM),
275 assumed to be a detrital remnant magnetization (DRM) acquired during the deposition of the sediment,
276 was determined after alternating field (AF) demagnetization. The rock magnetic properties were

Mis en forme : Exposant

Mis en forme : Exposant

Mis en forme : Exposant

277 investigated on u-channels from measurements of low-field susceptibility, acquisition and
278 demagnetization of ARM and IRM, coupled to thermomagnetic, hysteresis curves and first order
279 reversal curves (FORC) on 9 discrete samples. The full protocol is detailed in the supplementary
280 material (Sup. Mat. D).

281 The age depth model of the AFA18-02 sequence was constrained by a combination of short-lived
282 radionuclides, ^{14}C measurements and seasonal ~~varve~~ laminae [visual and microscopic](#) counting along the
283 core sequence. A continuous sampling step of 10 cm was applied over 173 cm of the AFA18-02
284 sequence to determine ^{210}Pb , ^{226}Ra and ^{137}Cs activities. The ^{14}C measurements were performed on 9
285 organic matter samples at the ARTEMIS facility, including 2 vegetal macro-remains and 2 fish bone
286 samples using ECHO-MICHADAS, the Micro Carbon Dating System of the LSCE laboratory ([Table](#)
287 [Tab. 1](#)).

288 **3.5 Rainfall-runoff modelling**

289 Observed streamflow time series at Tendaho Lake were extracted as daily timesteps from the GRDC
290 dataset (*station ID: 1577603, 11.683 N, 40.950 E, catchment area: 62 088 km², owner of original data:*
291 *Ethiopia - Ministry of Water Resources, Hydrology Department*). This time series is only available for
292 the 1990-2004 period, with numerous missing data during the 1994-1996 and the 2003-2004 periods.

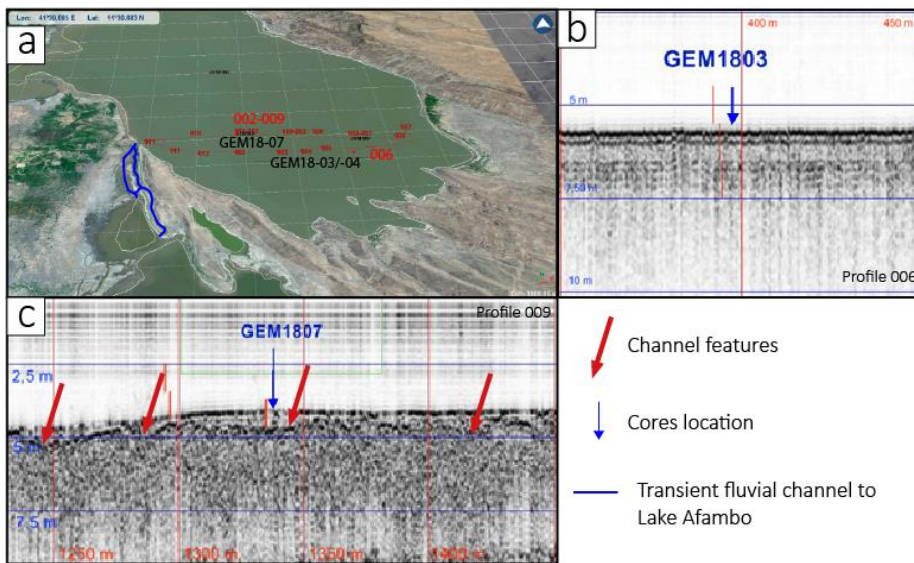
293 To extend the temporal extension of the streamflow series, a rainfall-runoff model was used. The
294 monthly rainfall-runoff model GR2M (Mouelhi et al., 2006) was used using the airGR R package (Coron
295 et al., 2022, 2017). This conceptual and lumped model needs two continuous climatic time series as
296 inputs, precipitation (P) and potential evapotranspiration (E). GR2M has two parameters that need to be
297 calibrated for each studied catchment (cf. model diagram in [Supp. Mat. B, Fig. S3](#)). The NOAA 20CR
298 (v3, Slivinski et al., 2019) climatic reanalysis was extracted over the Awash River catchment at Tendaho
299 Lake to generate a monthly time series of precipitation and air temperature over the 1836-2015 period.
300 A monthly potential evapotranspiration time series was then estimated using the 20CR air temperature
301 time series and the Oudin et al. (2005) formula. The model parameters were automatically calibrated
302 using the Nash and Sutcliffe (1970) objective function over the 1990-2014 period, with an initialization
303 of the model reservoirs during the 1980-1989 period. Finally, the GR2M model parameters obtained for
304 the Awash River at Tendaho Lake were used over the 1836-2015 period to simulate streamflow over
305 this period.

306 **4 Results**

307 **4.1 Seismic reflection imagery on Lake Gemberi**

308 Our chirp profiles provide a display of the bathymetry of Lake Gemberi for the first time. The average
309 measured water depth is 3 m with a maximum of 6 m in the southern part of the lake. Afambo Lake is

310 deeper, with a maximum depth of 18 m. The shallow depth (3 m on average) and very gentle slope of
 311 Lake Gemeri are consistent with its location in the prodeltaic area of the Awash Plain.
 312 Unfortunately, seismic penetration in Lake Gemeri is reduced to a few decimetres. Within the central
 313 and eastern parts of the lake, an approximately 80 cm-thick upper sheet drape unit lies on a low-
 314 amplitude reflector parallel to the lake bottom (profile 006, Fig. 2a, b). On the western part of the Gemeri
 315 Lake, the upper sheet drape unit lies on a relatively strong amplitude reflector displaying a succession
 316 of small highs and lows (few meters to tens of meters wide and a few decimetres deep) showing the
 317 morphology of an erosional surface (profile 009, Fig. 2c). The succession of highs and lows along this
 318 erosional surface correspond to small channels indicating periods of drying of the lake. Below these
 319 reflectors, an extensive acoustic turbidity facies showing similarities with gassy facies (Bertin and
 320 Chaumillon, 2005; Garcia-Gil et al., 2002) is observed. Five measurements of total organic carbon from
 321 core GEM18-03 on 2 m of sediment indicate values of approximately 8.5% (Sup. Mat. E), which
 322 suggests that the gas could have come from the decomposition of organic matter (algae or upper
 323 vegetation) in the lake. The presence of gas in the Lake Gemeri sediment is likely, given the high organic
 324 productivity in this lake and the high content in organic matter in the sampled sediments and
 325 sequestration of organic matter that often occurs in anoxic fine sediments (Bertin and Chaumillon, 2005;
 326 Garcia-Gil et al., 2002; Roussel et al., 2009).
 327



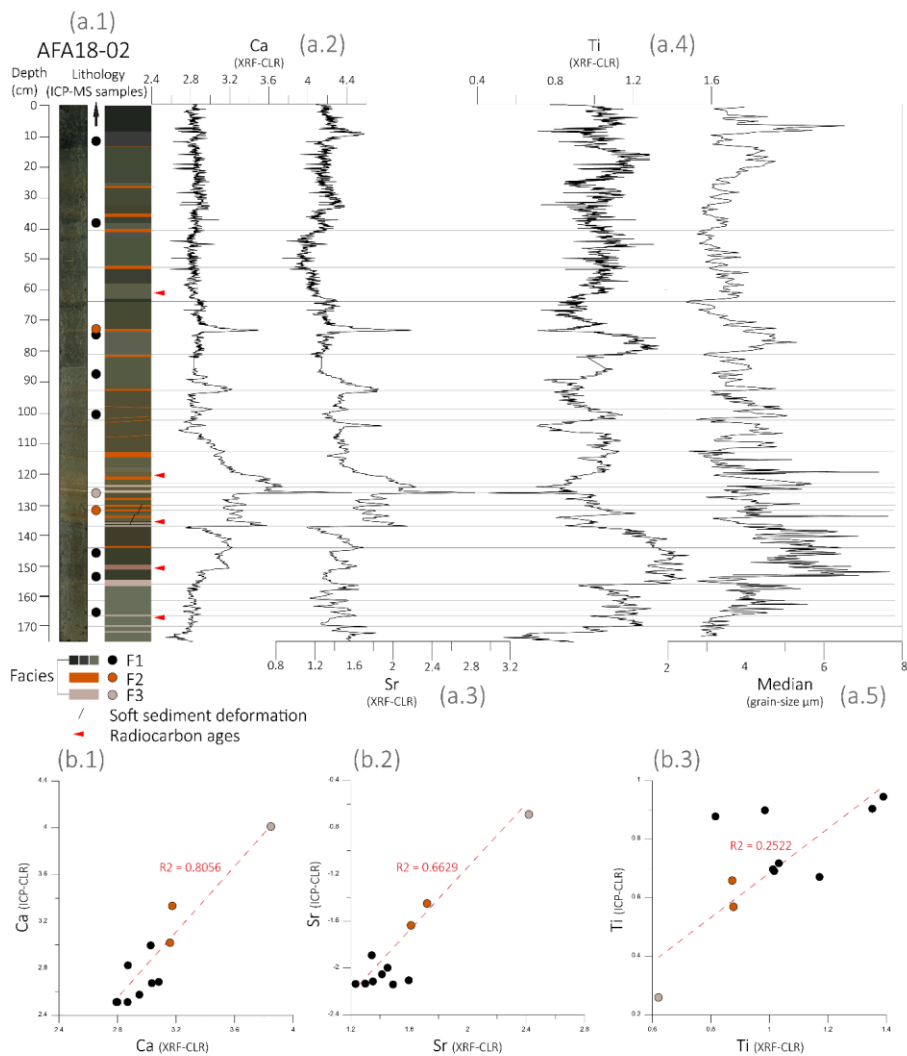
328
 329 **Figure 2:** Seismic reflection imagery on Lake Gemeri: a) 3D satellite image projection of southern Lake Gemeri (LANDSAT)
 330 with the location of the seismic profiles and of the cores reported in Figs. b and c; b) 006 seismic profile with the location of
 331 GEM18-03 core (blue arrow); c) 009 seismic profile with the location of GEM18-07 core (blue arrow) and of channel features
 332 (red arrows).

333 4.2 Sedimentology and geochemistry results

334 4.2.1 AFA18-02

335 The 173 cm-long sediment of AFA18-02 consists of undisturbed laminated sediments showing a clay-
336 silty texture (Fig. 3a.1). A median size of 3 and 7 μm was measured at 2 mm resolution along the 173
337 cm of the core, indicating that the lake's sedimentation did not record any extreme coarse or erosional
338 event (Fig. 3a.5). Along the core, the first striking characteristic of this sequence is the succession of a
339 couple of distinct facies systematically composed of brownish-grey coloured pluri-centimetric layers
340 (Facies-1; F1) alternating with orange/brown coloured pluri-millimetric layers (Facies-2; F2) and
341 sometimes associated with millimetric white beds (Facies-3; F3, Fig. 3a.1, 4b.1). Thirty-two couplets
342 were hence identified, over the entire 173 cm sediment sequence.

343 The major element distribution measured for 11 discrete samples (Tab. 1) indicates ~~SiO₂-SiO₂~~ values
344 oscillating between 25 and 46%, TiO₂ values between 0.7 and 1.7% and a high concentration in iron of
345 approximately 8%. Carbonate content values oscillate between 6 and 24% (Tab. 1). From the discrete
346 samples, the coefficient of correlation between Ca and Sr is $R^2 = 0.97$. This suggests that the source of
347 the carbonaceous component does not change along the 173 cm. Thanks to PCA analyses, 3 geochemical
348 end members from Dim.1 (53,67%)/Dim.2 (23,43%) were differentiated (Fig. S4): The first one (EM1)
349 yields major elements Al, Si, Fe, Ti, K, Zr and Mn with high positive loading on Dim1. The second end-
350 member (EM2) gathers elements composing carbonates (Ca and Sr) and elements involved in the
351 evaporitic succession of minerals (S, Mg, Na) with high positive loading on Dim2 and positive loading
352 on Dim1. The third end-member (EM3) includes only Br negative loading on Dim1 and Dim2, which
353 is often used as a proxy for autochthonous organic matter in lakes (Bajard et al., 2016; Lefebvre et al.,
354 2021). The PCA factor map ascribes F1 layers into the EM1 area and the F2/F3 layers into the EM2
355 area (Fig. S5). Consequently, we selected Ti, Sr, and Ca to geochemically characterize the F1 and F2/F3
356 facies. A good plot correlation between CLR transform XRF and ICP-MS measured elemental values
357 (Fig. 3b) provides reliable Sr and Ca XRF data to geochemically characterize the three different
358 sedimentary facies along the core sequence. F1 is composed of microlaminated clays enriched in Ti, Si
359 and Fe elements (Fig. 3b.3). The F1 thickness varies substantially along the core, with an average
360 thickness of ~3 cm between 173 and 137 cm, a thickness of ~1 cm between 137 and 120 cm, a thickness
361 of 3.5 cm between 120 and 80 cm, and a thickness of ~9 cm between 80 and 0 cm. F2 (0.5-1 cm
362 thickness) is composed of microlaminated clay, diffused secondary carbonate impregnations (sparite)
363 and sporadic Fe-Mn nodules. Geochemically, the F2 layers are slightly enriched in Ca and Sr elements
364 (Fig. 3a, 3b). F3 (0.3-0.5 cm thickness) is composed of a massive-to-microlaminated micritic/sparitic
365 matrix (Fig. 7b.1) strongly enriched in Ca and Sr elements (Fig. 3a, 3b, 7b.1). Soft sediment deformation
366 has been observed between 130 and 140 cm, evident in sub-vertical microfaults along the laminae,
367 showing a max deformation offset of ~3mm.



368
 369 **Figure 3:** Geochemical (XRF and ICP-MS) and sedimentological results on AFA18-02 core: **a.1**) Picture and lithology with
 370 the location of the sampling areas for ICP-MS analyses (dots); **a.2**) Ca XRF-(CLR) values; **a.3**) Sr XRF-(CLR) values; **a.4**) Ti
 371 XRF-(CLR) values; **a.5**) Grain size median; **b.1**) Correlation plot between Ca XRF-(CLR) and ICP-MS-(CLR) values; **b.2**)
 372 Correlation plot between Sr XRF-(CLR) and ICP-MS-(CLR) values; **b.3**) Correlation plot between Ti XRF-(CLR) and ICP-
 373 MS-(CLR) values.

374 Grain size distributions indicate three general dominant modes, one sorted clay mode at approximately
 375 1 to 2 μm , one well-sorted mode at approximately 19 μm , and the third is less dominant and lies in the
 376 sortable silt range at approximately 50 μm (Fig. 4b.3).

377 F1 layers present pronounced 1-2 μm and 50 μm modes, with the second represented mode at 19 μm .

378 F2 and F3 are well sorted at approximately 40 and 126 μm .

Dept (cm)	F	Na2O	MgO	Al2O3	K2O	CaO	TiO2	MnO	P2O5	SiO2	Fe2O3 (T)	Cr	Ni	Ba	Zr	Sr
		%	%	%	%	%	%	%	%	%	%	ppm	ppm	ppm	ppm	ppm
12	F1	1,97	4,62	13,13	1,85	6,30	1,50	0,10	0,28	45,80	9,57				271,65	423,40
39	F1	1,69	4,44	12,79	1,83	6,27	1,21	0,11	0,28	43,42	8,67	71,83	70,30	306,67	266,19	430,11
72	F2	1,32	4,35	10,60	1,43	14,16	1,06	0,11	0,26	36,48	7,30	59,87	56,34	371,84	221,51	847,12
73	F1	1,61	4,17	12,55	1,83	7,51	1,48	0,12	0,27	42,86	8,73	72,51	61,19	319,30	268,68	450,51
90	F1	1,39	4,08	11,78	1,92	8,37	1,14	0,10	0,26	42,62	8,26	72,86	62,70	287,74	254,22	480,19
100	F1	0,69	3,34	12,12	1,47	9,47	1,13	0,17	0,26	41,62	8,21	71,16	66,15	300,95	247,09	397,81
127	F3	0,96	5,28	6,67	1,01	23,79	0,67	0,14	0,19	25,11	4,57	39,57	40,49	399,08	136,28	1545,29
132	F2	1,34	4,93	10,58	1,53	10,39	1,24	0,11	0,25	37,96	7,42	67,73	62,20	351,79	227,72	706,21
148	F1	1,65	4,18	12,78	1,86	8,08	1,69	0,14	0,28	43,70	8,89	83,73	65,71	367,12	263,87	505,26
152	F1	1,58	4,47	12,64	1,89	6,93	1,55	0,12	0,26	43,45	8,82	82,59	63,67	329,38	266,35	454,91
168	F1	1,38	5,81	11,69	1,78	5,99	1,13	0,10	0,23	41,84	7,80	69,70	63,29	285,02	246,98	523,07

Tab 1: Major and trace element concentrations of the AFA18-02 core; F = Facies.

380

381 4.2.2 GEM18-03/04

382 The sediment of GEM18-03/04 is homogeneously clayey ($Q_{50} = \sim 2.4 \mu\text{m}$) and dark brown in colour
 383 (Fig. 5) all along its 220 cm. The first 15 cm are highly liquefied, presenting a clayey texture with slight
 384 laminations. Between 19 and 40 cm, we note the presence of polyhedral clay structure and rootlets
 385 poress. Between 38 and 222 cm, we observed a homogenous clay texture interbedded by seven layers
 386 of lacustrine shells (*Melanoides tuberculata*), leading to a visible change in porosity at approximately
 387 62 to 67 cm, 80 cm, 90 cm, 112-114 cm, 124 cm and 140 cm (Fig. S19).

388 The major element distribution (measured for 5 samples by ICP-MS, Table S1, S2) indicates SiO₂-SiO₂
 389 values between 42 and 49% and TiO₂ values between 1.2 and 1.5%. The carbonate content values
 390 oscillate between 5 and 10% (Table S1, S2). The plots Si versus Al and Al versus Ca indicate an
 391 anticorrelation between terrigenous and carbonated materials; (Fig. S20), suggesting that the carbonate
 392 particles mainly originated from the lake and not from the terrigenous fraction supplied by the Awash
 393 flood. Similarly, the coefficient for Ca versus Ti is anticorrelated, consequently we will represent the
 394 ratio of terrigenous/authigenic sediment components using the Ti/Ca ratio_ (Croudace and Rothwell,
 395 2015).

396 The evolution of the Log(Ti/Ca) ratio defines 5 geochemical units (Fig. 5b.1): Unit 1 (0 to 19 cm) is
 397 characterized by a gradual increase in Log(Ti/Ca) values. Unit 2 (40 to 19 cm) is characterized by a
 398 gradual increase in siliciclastic elements; Unit 3 (115 to 40 cm) presents an abrupt decrease in
 399 Log(Ti/Ca) at its base, followed by a progressive increase in Ti; Unit 4 (210 to 115 cm) is characterized
 400 by a high lithogenic contribution; Unit 5 (222 to 210 cm) presents a high carbonate content. Between
 401 38 and 222 cm, seven shell beds are characterized geochemically by an increase in Ca and Sr values
 402 (Fig. S19).

403 **4.3 Chronology**

404 **4.3.1 Age model of Lake Afambo sediments**

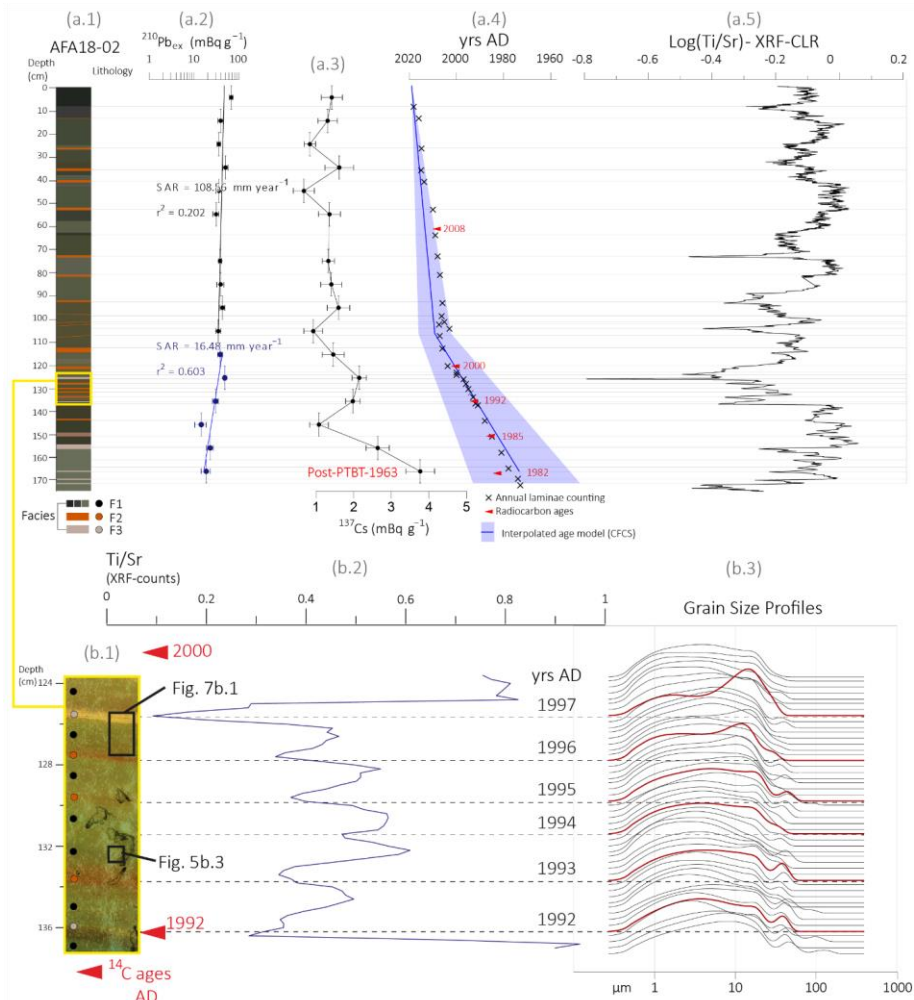
405 The 173 cm long AFA18-02 sediment was measured using gamma spectrometry to build an age model
 406 based on short-lived radionuclides (Fig. 4a.2, 4a.3). The ²¹⁰Pb excess profile first shows a slow decrease
 407 from the top to 105 cm and then a more rapid decrease between 105 and 170 cm until an activity of 26
 408 mBq.g⁻¹. The use of a logarithmic scale to plot these data underscores a poorly constrained (r²=0.2,
 409 related to very high sedimentation rate leading to low activity decreases) single-point alignment that
 410 shows a constant sedimentation rate of 108 mm.yr⁻¹ for the first 105.8 cm and a better constrained
 411 (r²=0.6) single-point alignment that shows a constant sedimentation rate of 16.5 mm.yr⁻¹ between 106
 412 and 170 cm. The change in sedimentation rate occurred in 2009 +/- 7 years. The ¹³⁷Cs profile shows an
 413 increase at the bottom of 4 mBq.g⁻¹. This peak could be associated with the end of maximum nuclear
 414 weapon tests in 1963 CE (Foucher et al., 2021; Fig. 4a.3).

Sample ID Depth (cm)	Lab ID	Material	Uncalibrated Age		Calibrated ages	
			BP ± yrs (bulk)	F ¹⁴ C ± (%)	2σ cal ADCE (probability)	Median cal ADCE
AFA18-02A-10.5-11	SacA57084	Bulk sediment	315 ± 30*			
AFA18-02A-44	SacA57085	Bulk sediment	640± 30*			
AFA18-02A-61	GifA20055/ECHo3328	Fish Bone		1.0456 ± 0.0029	[2008.88 - 2009.58] (30.3%)	2008
AFA18-02A-61	SacA59130	Bulk sediment	610 ± 30*			
AFA18-02A-76	SacA57086	Bulk sediment	365 ± 30*			
AFA18-02B-8-8.592	SacA57087	Bulk sediment	165 ± 30*			
AFA18-02B-35-39118-122	GifA20052/ECHo3259	Vegetal micro remains		1.0940 ± 0.0179	[1993.78 - 2007.1] (90.3%)	2000
AFA18-02B-50.5-51-134.5-135	SacA57088	Bulk sediment	post 1950*			
AFA18-02B-51-53134-136	GifA20053/ECHo3260	Vegetal micro remains		1.1364 ± 0.0123	[1989.86 - 1996.94] (89.3%)	1992
AFA18-02B-66.5-149.5	GifA20056/ECHo3327	Fish Bone		1.2069 ± 0.0031	[1984.82 - 1986.45] (52.8%)	1985
AFA18-02B-67150	SacA59131	Bulk sediment	320 ± 30*			

AFA18-02B_82.5-83.5 165.5-166.5	GifA20054/ECHo3261	Vegetal micro remains		1.2357 ± 0.0133	[1980.8 - 1982 1985.76A] (59.9%)	1982
AFA18-02B_81.5-82 165.5-166	SacA57089	Bulk sediment	post 1950*			

415 **Tab 2:** List of radiocarbon ages on bulk sediment (*), vegetal micro remains and fish bone material. Ages with * are
416 rejected. Calibration curve NH2 (Hua et al., 2013).

417 Among the 13 samples for ¹⁴C ages (Tab. 2), the confrontation with the ²¹⁰Pbex model shows that the
418 ¹⁴C age measured on the bulk sediment organic matter was older, so these ages were systematically
419 rejected (* in Tab. 2). The older ages could be explained by the contamination of reworked micro-
420 organic matter particles from the Awash River catchment. The aging of radiocarbon dates on bulk
421 organic matter in large fluvial systems, such as the Awash River Basin, is often attributed to the
422 remobilization of fine organic particles from older deposits and soils eroded along the hydrographic
423 catchment. These particles are then deposited into terrigenous/detrital lacustrine sediments. In the case
424 of Afambo Lake sediments, the ages of bulk organic carbon exhibit an aging effect ranging between
425 approximately 100 and 600 years. Considering that the organic matter originates from flood deposits
426 during the monsoonal season (F1 facies), the hypothesis of remobilized fine particles is the most
427 probable explanation. A number of ¹⁴C analysis were measured on fish bones and on vegetal micro
428 remains obtained from the micro sampling materials (Fig. S21 and S22). The five ages measured from
429 fish bone and vegetal micro remains are consistent with the ²¹⁰Pb-derived chronology and are considered
430 viable as part of the age model (Fig. 4a.4). 32 F1-F2/3 laminae couplets were identified and counted ~~in~~
431 ~~the F1 and F2 couplets (Fig. 5d)~~, which provides a 106 mm.yr⁻¹ sedimentation rate that is highly
432 comparable with the rate derived from the CFCS model (108 mm.yr⁻¹; Fig. 4a.2). Thus, the ²¹⁰Pb-derived
433 age model confirms that a very high sedimentation rate compatible with the F1 layers could correspond
434 to one season of river-borne discharge.

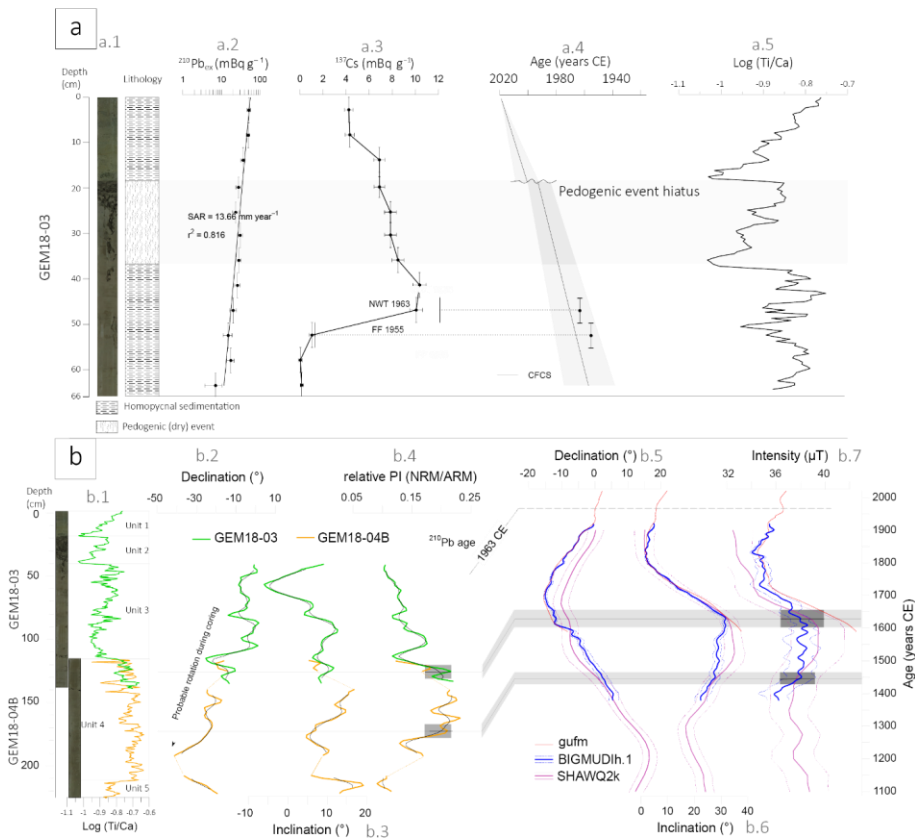


435
 436 **Figure 4:** Age model of the AFA18-02 sequence: **a.1**) lithology; **a.2**) ^{210}Pb activity profile ($\text{mBq}\cdot\text{g}^{-1}$); **a.3**) ^{137}Cs activity profile
 437 ($\text{mBq}\cdot\text{g}^{-1}$); **a.4**) interpolated CFCS age model with annual laminae counting (crosses) and radiocarbon ages (red arrows); **a.5**)
 438 XRF $\text{Log}(\text{Ti}/\text{Sr})$ ratio transformed with a Centred Log Transformation package (Weltje and Tjallingii, 2008); **b.1**) focus on
 439 124-140 cm F1-F2/F3 couple counting; **b.2**) XRF Ti/Sr (124-140 cm) ratio curve with radiocarbon ages (red) and yrs
 440 AD/laminae counting; **b.3**) 124-140 cm grain size profiles (each 2 mm).

441 4.3.2 Age model of Lake Gemeri

442 The upper 66 cm sedimentary sequence of the GEM18-03 core was measured using gamma
 443 spectrometry to build an age model based on short-lived radionuclides (Fig. 5a.1, 5a.2). The ^{210}Pb ex
 444 profile shows a gradual decrease from 51.8 to 7 $\text{mBq}\cdot\text{g}^{-1}$. The use of a logarithmic scale to plot these
 445 activities underscores a well-constrained ($r^2=0.8$) single-point alignment that shows a sedimentation rate
 446 of 13.66 $\text{mm}\cdot\text{yr}^{-1}$ for the first 66 cm (Fig. 5a.2). The ^{137}Cs profile reaches a clear peak between 42 and
 447 48 cm with a maximum activity $>10 \text{ mBq}\cdot\text{g}^{-1}$. This peak is attributed to the maximum nuclear weapon

448 tests in 1963 CE (Foucher et al., 2021) and is in accordance with the sedimentation rate derived from
 449 the ^{210}Pb ex profile (Fig. 5a.2). Above this peak, ^{137}Cs activities slowly decrease, which suggests a large
 450 catchment area with input of ^{137}Cs already deposited in surface soil and transported by active annual
 451 floods (Fig. 5a.3). With the aim to provide a reliable chronology, sedimentary-pedogenic hiatus between
 452 1991 and 1997 has been removed from the age model (Figs. 5a.4, 6a.2).
 453 Among the 13 ^{14}C age samples (Sup. Mat. I), the confrontation with the ^{210}Pb CFCS-derived chronology
 454 shows that the ^{14}C ages measured on organic matter are older by several thousands of years, and are
 455 therefore rejected with regard to the age model, such as is the case for 8 ages on bulk sediment for the
 456 Afambo core age model (Tab. 2). The five ages measured on lacustrine shells (*Melanoides tuberculata*;
 457 Murray, 1975) are still older than expected except for the age at 48.5 cm (Fig. S23).



458
 459 **Figure 5:** a.1) GEM18-03 upper section (first 66 cm) picture and lithology, a.2) ^{210}Pb ex and a.3) ^{137}Cs profiles, NWT=Nuclear
 460 Weapons Tests; FF= FF 1955: first identification of 137 Cs in 1955; a.4) CFCS interpolated age model and a.5) Log(Ti/Ca)
 461 XRF count intensity. b.1) GEM18-03/04B composite section with Log(Ti/Ca) XRF count intensities; correlation between b.2)
 462 relative palaeo-intensity, b.2) inclination and b.2) declination measured on GEM18-03/04B with the b.5 to b.7) prediction at
 463 Lake Gemi of three geomagnetic global models, BIGMUD1h.1 (in blue, Arneitz et al., 2021), gufm (in red, Jackson et al.,
 464 2000) and SHAWQ2k (in purple, Campuzano et al., 2019). BIGMUD1h.1 and SHAWQ2k.1 models are plotted with their 1- σ
 465 uncertainty envelope. The correlation is preferentially based on the BIGMUD1h.1 model (see text). For GEM18-03/04B, green
 466 and orange thick lines are raw results on GEM18-03 and GEM18-04B sections, respectively, while the thinner black curves

467 *show the variation after smoothing with 8-cm sliding windows. The two chronological tie-points are given by RPI, while the*
468 *secular variation of declination, and to a lesser extent of inclination is likely masked by disturbances during coring.*

469 To better constrain the age model and investigate the sedimentation rate below the first 66 cm dated by
470 short-lived radionuclides, we performed palaeomagnetic measurements with the objective of providing
471 chrono-markers in accordance with the palaeosecular variation in the geomagnetic field over the last
472 millennium (Fig. 5b; Crouzet et al., 2019). The rock magnetic and palaeomagnetic results are detailed
473 in Sup. Mat. D. All rock magnetic results converge towards a homogeneous ferromagnetic mineralogy
474 below 40 cm, composed of almost pure magnetite of relatively fine grain size (pseudo single domain).
475 As the concentration in magnetic grains also does not vary significantly along the core, the magnetic
476 properties are very favourable to the determination of the relative palaeointensity (RPI; Fig. 5b.4). The
477 RPI results with the three possible normalizers (intensity of anhysteretic remnant magnetization ARM,
478 intensity of isothermal remnant magnetization IRM (low-field susceptibility)) are consistent, giving us
479 confidence in our RPI estimation even though it is based on only one core (Fig. 5b). The variations in
480 declination, inclination and RPI below 40 cm are plotted in Figs. 5b.2 and 5b.3. They are compared to
481 the prediction at Lake Gemeri of three geomagnetic global models: gufm (Jackson et al., 2000),
482 SHAWQ2k (Campuzano et al., 2019) and BIGMUDIh.1 (Arneitz et al., 2021; Figs. 5b.5 and 5b.6).

483 The correlation between the GEM18-03/04B results and the model is not straightforward. However,
484 ¹³⁷Cs and ²¹⁰Pbex results from the top of the core allow us to propose a more solid chronological
485 framework of the sedimentary sequence. The almost continuous decrease in declination along the core
486 could suggest that the 190-222 cm depths could correspond to circa 1700 ~~AD-CE~~. However, the
487 amplitude of the decrease at approximately 40° is much larger than that in the models (approximately
488 15°), and we strongly suspect that the declination record is biased by a slight progressive rotation feature
489 during coring. Short inclination oscillations in the core are not recognized in the model. Neither the
490 inclination minimum approximately 1840 ~~AD-CE~~ nor the previous fast and regular decrease from 1630
491 ~~AD-CE~~ are clearly visible in GEM18-03/04B. Higher inclination values are in accordance with the
492 model between 130 and 160 cm.

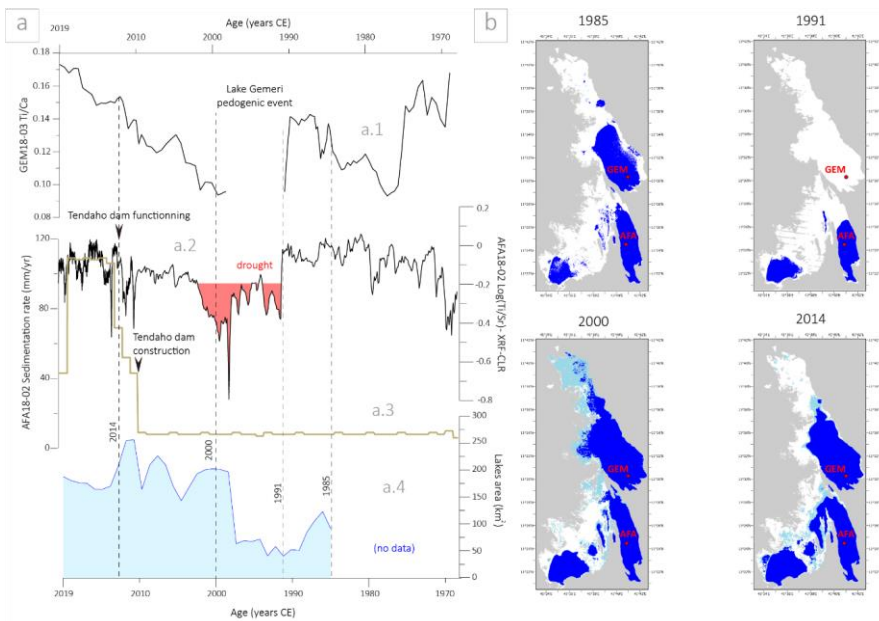
493 The period of higher intensity between the middle of the 15th c. and the first half of the 17th c. ~~AD-CE~~
494 appears to be recorded between 170 cm and 125 cm in GEM18-03/04B. This feature could provide two
495 chrono-markers to establish the age model, 120-130 cm corresponding to 1600-1650 CE and 167-177
496 cm to 1430-1460 CE. These two proposed tie points are rather consistent with inclination variations
497 because higher values of this parameter are observed in the two ranges of depth and age. The values of
498 correlated depths and ages should be considered approximate regarding the envelope error on the model
499 and because the predictions of global models are generally less reliable in intensity than in declination
500 and inclination (e.g., Brown et al., 2021). Palaeomagnetism measurements based on a single core cannot
501 provide a solid and high-resolution age model. However, the correlation with short-lived radionuclide
502 measurements on GEM18-03 and with the AFA18-02 age model allows us to propose some reliable
503 links with the Awash River hydro-sedimentary chronicles which are at decennial resolution. The

504 palaeomagnetic measurements provide confirmation that ^{14}C ages from GEM18-03/04B are too old, and
 505 that these sediments do not exceed the last millennium.

506 **4.4 Changes in water surface area at Lakes Gemberi and Afambo, 1985 -**
 507 **2019**

508 Since 1984, Landsat satellite image data have indicated that Lake Afambo experienced several
 509 hydrological fluctuations without a complete drying of the lake. In contrast, Lake Gemberi partially dried
 510 up starting in 1984, with a total drying up of the lake between 1990 and 1998 (Fig. 6, see Figs. S26 to
 511 S28 for details). Then, between 1999 and 2000, the lake was completely refilled. Comparisons between
 512 hydrological, geophysical, sedimentological and geochemical data will be discussed in the next
 513 paragraphs- Palaeolimnological and hydrological results from satellite image analyses might be not
 514 perfectly linearly correlated due to sedimentary avulsions and earth surface processes along the river
 515 course and between the two lakes (Phillips, 2003). Additionally, such offset can be attributed to the
 516 combined $^{210}\text{Pb}/^{137}\text{Cs}$, counting couplets and radiocarbon age model errors which can span from 1yr to
 517 7yrs.

Mis en forme : Exposant
 Mis en forme : Exposant



519 **Figure 6:** Hydrosedimentary variability of Lakes Gemberi and Afambo during the last fifty years: **a.1** Ti/Ca XRF ratio of
 520 GEM18-03 sequence; **a.2** Ti/Ca XRF ratio of AFA18-02 sequence; **a.3** AFA18-02 sedimentation rate; **a.4** lakes-level area
 521 changes since 1985, Afambo + Gemberi; **b**) map representation of lake area changes in 1985, 1991, 2000 and 2014 CE; white
 522 = no water, light blue = 1 month water (temporary water), blue = 12 months of water (permanent water), grey = no data.
 523

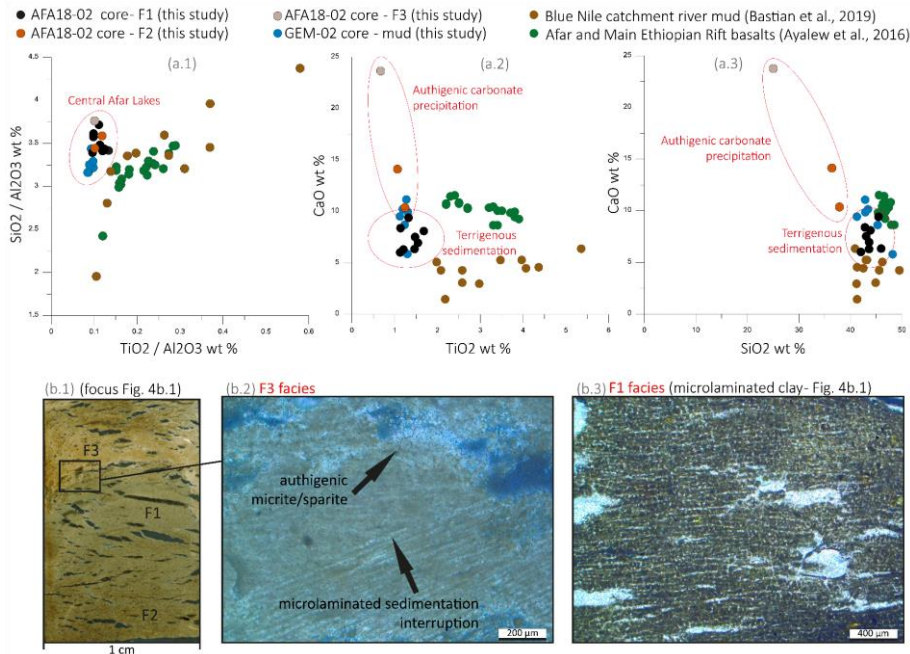
524 **5 - Discussion**

525 **5.1- AFA18-02 F1 and F2 significance**

526 **5.1.1 – F1 interpretation**

527 In the geological context of the Afar depression and Main Ethiopian Rift (MER), Si, Ti and Ca wt %
528 values of AFA18-02 and GEM18-03/-04B are compared with the same values of 11 mud samples from
529 the Blue Nile headwaters catchment (Bastian et al., 2019) and with 20 basalt samples from the Afar and
530 MER regions (Ayalew et al., 2016), corresponding to the sources of the Awash River catchment (Fig.
531 7). The Afar lake sediments are well-ranged in SiO₂ wt% values and ~~partially partially overlap~~ included
532 withⁱⁿ the TiO₂ wt% values of the Ethiopian trap basalts and sediment sources, indicating that the origin
533 of the terrigenous inputs into the lakes is mainly represented by the solid discharge of the Awash River
534 catchment. The ~0.1% offset between the Afar lake sediments and the Ethiopian river sediments and
535 basalts can be attributable to a granulometric sorting effect. Similarly, the lithogenic signature
536 originating from the erosion of stratoid basalt series along the Awash River catchment is confirmed by
537 the ferromagnetic mineralogy of GEM18-03/-04B composed of almost pure magnetite (see section
538 §4.3.2 and Sup. Mat. D).

539 Thick layers, high organic matter content, coarser grain size (D90 peaks of 25-30 μm, ~~Fig. 9e~~) dominated
540 terrigenous elements (Si, Ti, Fe, Fig. 7a; EM-1 PCA, Sup. Mat. C) characterize the F1 facies, interpreted
541 as a product of sedimentary load inputs from the Awash River during the wet season, which is associated
542 with the increase in monsoonal precipitation between March and August over the catchment sources
543 located on the Ethiopian Highland (~~Fig. 1D~~). The F1 patterns indicate that the ~~total water and~~ solid load
544 inflow during the wet season corresponds to the formation of a particle suspended plume into the lake
545 waters. The lack of erosion features, the disconnection from deltaic geomorphic dynamics and the
546 regular mode of sedimentation (seasonal) indicate that Afambo is a basin characterized by yearly cyclic
547 hydrosedimentary functioning.



548
 549 **Figure 7:** Geochemical and microscopic analyses and interpretation of F1, F2 and F3 facies: **a.1, 2, 3** SiO₂/TiO₂, CaO/TiO₂
 550 and CaO/SiO₂ plots respectively, of Central Afar Lake sediments (black, orange and grey dots; This Study), Blue Nile
 551 catchment river muds (green dots; Bastian et al., 2019) and Afar and Main Ethiopian Rift Basalts (brown dots; Ayalew et al.,
 552 2016). **b.1)** Focus scan of this section 125-128 cm depth of AFA18-02 core (XPL); **b.2)** Microphoto of F3 facies (XPL); **b.3)**
 553 Microphoto of F1 facies (PPL).

554 5.1.2 – F2/F3 interpretation

555 The F2 and F3 facies appear to be enriched in CaO of ~5-10 wt% and ~24 wt%, respectively, and in Sr
 556 of ~800 ppm and ~1500 ppm, respectively, as a part of EM-2 of XRF PCA (Sup. Mat. C). Difference
 557 between F2 and F3 is related to the CaO content: F2 is whitish-brown with a CaO ranged between ~10
 558 and ~15 wt%; F3 is white with a ~24 wt% CaO content. Microscopically, such enrichment is observable
 559 in the precipitation of sparitic and micritic minerals, showing an interruption of the microlaminated
 560 structure typical of F1 (Fig. 7b.2), and suggesting a sedimentation mode and carbonated mineral
 561 formation disconnected from the Awash River terrigenous inputs and suspension/sedimentation of fine
 562 particles in the lake. Moreover, F2 and F3 are clearly disconnected from the regional mineralogical
 563 source cortege (Fig. 7a.2 and 7a.3), indicating how such minerals originate from the lacustrine
 564 authigenic activity. Under high evaporation conditions during the dry season, sparitic minerals can be
 565 produced directly by chemical or biogenic precipitation into the lake.

566 Authigenic minerals precipitate when the evaporation rate exceeds the water inflow rate into the lake,
 567 leading to a switch from a terrigenous sedimentation pattern to the carbonate mineral precipitation mode.
 568 Considering high evaporation rates over the Lake Abhe basin (PE ~2000 mm/yr, Fig. 4E) which are
 569 concentrated during the dry season where there is low water inflow, authigenic precipitation of Ca and

570 Sr can represent the direct results of highly saturated waters and the related evaporative processes
571 (Cohen, 2003; Kylander et al., 2011; Martín-Puertas et al., 2011). Indeed, Ca and Sr are related to intra-
572 lake precipitation of CaCO₃ with Sr and Ca substitution. This substitution occurs when the chemical
573 concentration of lake waters reaches the point of carbonate saturation, as when lake waters are submitted
574 to a lowering of lake levels (Cohen, 2003). Accordingly, lake surface analyses show that enriched Ca
575 and Sr layers are concomitant with a lowering in Gemer and Afambo lake levels (Fig. 6a.2).
576 Consequently, F2 and F3 have been interpreted as the occurrence of the dry seasons along the Awash
577 River catchment over the last 50 years, and Ca and Sr elemental values can be used as a marker of
578 drought intensity.

Mis en forme : Indice

579 **5.2 – Hydro-sedimentary mechanisms between Gemer and Afambo Lakes**

580 Despite their proximity, Gemer and Afambo Lakes present divergent patterns of sedimentation,
581 suggesting interdependent and complementary hydro-mechanisms. Located on the prodeltaic front,
582 Lake Gemer is the first and main receiver of the Awash River waters and sediment, which then overflow
583 into the Afambo basin (Fig. 1). Surprisingly, the ²¹⁰Pbex activities of both lakes indicate a higher average
584 sedimentation rate in Lake Afambo (~10 cm.yr⁻¹) than in Lake Gemer (~1.36 cm.yr⁻¹).

585 Lake Gemer is characterized by a shallow water column (average of ~3 m depth measured during the
586 coring and seismic reflection imagery acquisition) in which the extension of the proximal seismic facies
587 into the central part of the basin is observed (Fig. 2). Such evidence suggests how the inputs of the
588 inflow waters create sediment plumes that have expanded in three dimensions from the tributary mouth
589 towards the basin floor. Furthermore, the main homogeneous (non-laminated) structure of the deposits
590 (Fig. 5) suggests the input of continuous turbid currents (no variability in density) from the Awash River
591 waters. Such specific depositional patterns (deposit spatial geometry and sedimentary structure) are
592 attributable to homopycnal-like sedimentation, in which the density of the suspended sediment flow is
593 equal to that of the lake water (Bates, 1953; Chapron et al., 2007). In the absence of water stratification,
594 homopycnal conditions imply the homogeneous mixing of river and lake waters throughout the whole
595 water column by advection processes (Ashley, 2002; Bates, 1953; Chapron et al., 2007). In terms of
596 depositional processes, the occurrence of a homopycnal plume implies a short residence time of water
597 and solid suspended loads in lake waters, leading to reduced sedimentation on the basin floor (Campos
598 et al., 1989) and the development of contrasting sedimentation patterns between proximal and distal
599 basins (Chapron et al., 2007, 2006). Accordingly, most of the solid load transits through Lake Gemer,
600 producing a low sedimentation rate and erosive facies observed from seismic profiles, which have not
601 been recognized in the distal Lake Afambo basin (Fig. 2c). Furthermore, the shallow water patterns of
602 Lake Gemer (~3 m average water-column depth) can promote the re-suspension of the bottom lake
603 sediments after the river floods or during wind-generated waves, reducing the sediment accumulation.

604 At 17 m water depth (coring site), Lake Afambo sediments show seasonal laminated structures (F1 and
605 F2/3). Facies alternation as well as the microlaminated structure documented in the F1 layers (Fig. 7b.3)

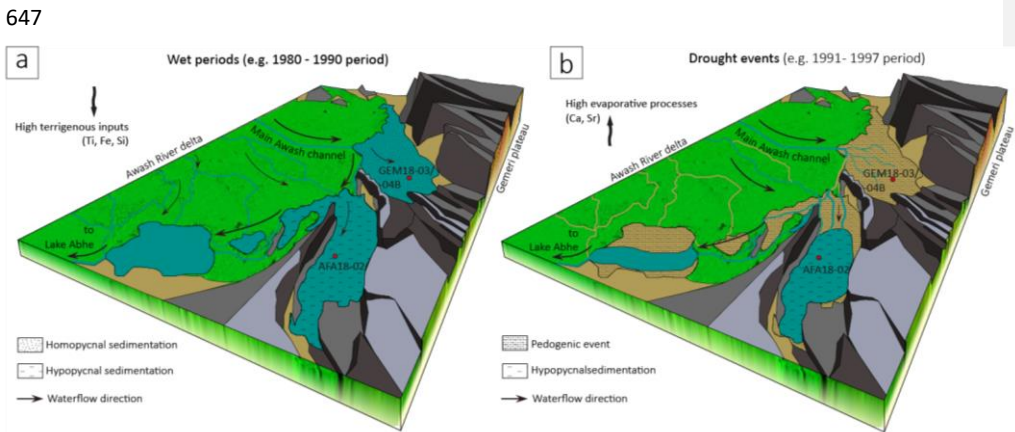
606 indicates the occurrence of rapid decantation processes shortly after each flood, thus suggesting slight
607 water column stratification and a difference between freshwater inputs and lake water density. Particle
608 sedimentation velocities calculated with the Stokes law confirm such observations, providing a mean of
609 ~3 days for the particles to sediment in Afambo lake (~~Sup. Mat. ETab. S3~~). Such sedimentary patterns
610 combined with the absence of erosive or turbiditic events suggest a hypopycnal character of the inflow
611 waters/solid load into Afambo Lake. Hypopycnal plume formation at the tributary mouth of Lake
612 Afambo can be made possible by the decrease in the current energy flow and by the loss of density of
613 the waterfront by the trapping of fine sediments into the deltaic marshes occurring between the two lakes
614 (Fig. 1). Accordingly, the <3.9 μm fraction is represented by 60-80% in Lake Gemeri and by 20-35%
615 in Lake Afambo (~~Sup. Mat. Figs. S24 and S25~~). Other factors that could influence the formation of
616 hypopycnal plumes in Afambo Lake are the reduced energy flow into the lake waters due to the
617 endorheic patterns of the basin (no outflow towards Lake Abhe) and a larger water-column depth.
618 The explanation of the general hydro-sedimentary modes of functioning of the two basins indicates **a**)
619 a first prodeltaic basin (Gemeri) with lower sedimentation rates, dominated clayey texture, erosive
620 processes and deltaic dynamics-dependant, which have recorded the general trends
621 (~~decennial/centennial~~) of hydrological fluctuations of the Awash catchment over a long period (~700
622 yrs) in our study; **b**) a second distal basin (Afabmo) with higher sedimentation rates, clayey texture and
623 seasonal F1 and F2/3 deposits, which records in high-resolution (interannual) the hydrological
624 fluctuations of the Awash River catchment during a short period (~50 yrs).

625 626 **5.3– Multi-centennial hydro-sedimentary trends from Lake Gemeri** 627 **sediments**

628 Similar to AFA18-02, PCA on XRF data of the Gemeri sequence (Fig. S6) show three main geochemical
629 end-members: the terrigenous one composed of Ti, Si, Al, K, Zr, Fe, Mn, and Mg; the evaporitic (Ca
630 and Sr); and the organic component (S and Br). Diachronic variations in these main components along
631 the GEM18-03/-04 core allow us to define two kind of periods: “Humid pluriannual periods” are
632 characterized by high terrigenous content such as Ti from high water flow activity of the Awash River.
633 Contrastingly, “drier pluriannual periods” are characterized by the enrichment of Ca and Sr element
634 values interpreted as evaporative processes as a result of higher evaporation and reduced water inflow
635 into the lakes (~~Fig. 8~~). Thanks to the composite short-lived radionuclides and palaeomagnetism age
636 model on the GEM18-03/04 sequence (~~Fig. 5b~~), we are able to discuss the general hydrological trends
637 (centennial resolution) for the period ranging between 1300 and 1964 CE.

638 Between 1300 and 1650 CE, relatively high and constant Ti/Ca ratio values were recorded (Fig. 5b.1).
639 This indicates how this period is characterized by high detrital inputs into the Lake Abhe basin, likely
640 induced by water inflow processes over the Awash River basin. Following a drop in Ti proxy between
641 1650 and 1750 CE, the catchment could have experienced a gradual increase in water and solid load

642 flow until 1979-1964 CE, as deduced from the increase in Fe, Ti and Si elemental content. The last
 643 decade (1968-1979-1964 CE) is thus characterized by higher solid load supplies compared to the
 644 following periods. Geomorphologically, during this timesuch decade, the Awash palaeo-delta was likely
 645 characterized by an anastomosing river network pattern that fed the prodeltaic lakes and marshes from
 646 the southwest to the northeast of the alluvial plain (Fig. 8a).



648
 649 **Figure 8:** Schematic interpretative model of hydro-sedimentary patterns of the Awash River delta (including lakes Gemeri and
 650 Afambo) during enhanced wet periods (a) and drought events (b).

651 **5.4 - ~50-year-long seasonal drought and flood chronicle from Lake**
 652 **Afambo**

653 In the AFA18-02 core, F1 and F2/F3 layers are interpreted as a result of the sedimentary interannual
 654 response of Central Afar Lake basins to wet and dry seasonal discharge of the Awash River. Thanks to
 655 the multi-proxy geochronological approach, we are able to propose a solid age model covering the
 656 period between 1969 AD-CE and 2019 AD-CE.

657 The aim of this section is to provide a wet and dry season magnitude ~~chronicle~~ chronicle for the last ~50
 658 years across the Awash River basin through a) the estimation of the wet season inflow intensity
 659 recognized in F1 layers and b) the estimation of drought/evaporitic process intensities recognized in dry
 660 season F2/F3 layers (see section §5.1 for the facies interpretation).

661 With the aim of reconstructing the intensity of the Awash River wet season intensities, we selected two
 662 proxies: the grain size and the thickness of the F1 layers. Thanks to well-established published data, we
 663 are able to propose an interpretation of the river energy discharge based on the grain-size data (e.g.,
 664 Campbell, 1998; Lapointe et al., 2012; Parris et al., 2010; Sabatier et al., 2022, 2017; Wilhelm et al.,
 665 2015). Indeed, the coarse grain size fraction (~~Q90D90~~ Q90D90) has been successfully used to track hydrologic
 666 conditions, particularly the transport capacity and the stream velocity during flood events, such as the
 667 intensity of past floods (Gilli et al., 2013; Molinaroli et al., 2009; Parris et al., 2010). Similarly, previous

668 studies interpret the thickness of flood deposits in lakes as the total volume of solid material transported
669 and deposited during flood events (Jenny et al., 2014; Schiefer et al., 2011; Wilhelm et al., 2015, 2012).
670 Chronologically corresponding to the duration of the monsoonal rainy season and in absence of
671 turbiditic layers or singular events deposition sedimentary patterns (e.g. flash floods). Assuming that the
672 F1 layers are not considered as the a result of a unique flood event but as the sum of flood events that
673 occurred during the wet season. Consequently, we can consider the F1 layer thickness and Q90D90
674 as proxies of the Awash discharge intensity in terms of flow energy and the volume of solid load that
675 occurred during the wet monsoonal period between March and August. In our case, the striking
676 similarities between D90 peaks and thickness of F1 layers (Fig. 9b, c) confirms the combination of
677 proxies for tracking the flood season intensities.

678 To reconstruct the intensity of the dry season, we use Sr and Ca elements (~~Fig. 3~~) and the Ti/Sr elemental
679 ratio (Fig. 9) as a marker of evaporative processes resulting from reduced water flow inputs, ~~and the~~
680 contraction of the lake surface ~~and high temperatures~~ as explained in detail in section §5.1.2. The
681 relationship between enhanced carbonate precipitation and drought intensity in Lake Afambo is evident
682 in the F3 layer at 126 cm, corresponding to the 1997 CE dry season (~~Fig. 4~~), in which the highest Ca
683 and Sr values recorded in the core correspond to the lowest lake level ever observed (~~Fig. 6~~) and the
684 strongest impact of El Niño that has ever been historically recorded over East Africa (Fig. 9; Palmer et
685 al., 2023).

686 The comparison between Ti/Sr, F1 thickness and D90 proxies (Fig. 9a, b and c) shows a strong
687 relationship between physicochemical authigenic processes (carbonate precipitation and Sr enrichment
688 linked to evaporative trends in the dry season) and the Awash River solid load inputs into the lake (linked
689 to the increase or the reduction of water flow at the yearly scale). Consequently, we are able to discuss
690 the variability of the wet seasons and drought intensities in the Central Afar region over the last ~50
691 years.

692 Between 1969 and 1979, a gradual increase in both F1 thickness and D90 indicates a decennial
693 intensification of wet season solid/liquid Awash river discharge, with two years of demarcated wet
694 season floods in 1976 and 1978. Decrease of Ti/Sr indicate an enhanced dry season in 1969, 1978 and
695 1979. Between 1980 and 1990, a general and constant trend of high river discharge was recorded with
696 enhanced floods in the 1981, 1982, 1988 and 1989 wet seasons. A pronounced drought was recorded in
697 1983/1984.

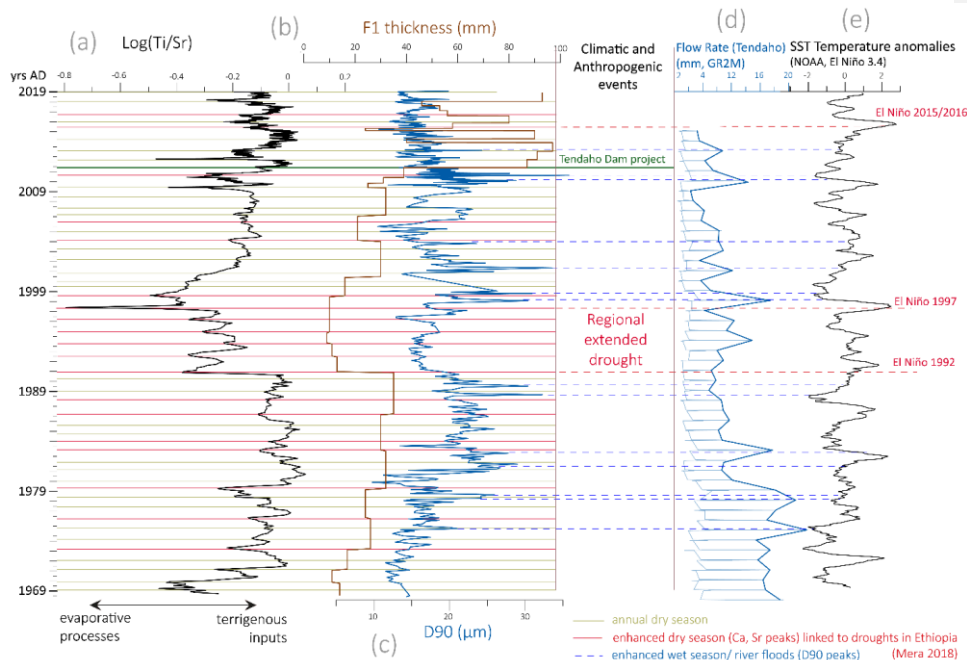
698 From 1991 to 1997, the occurrence of an abrupt lowering thickness of F1 and low and constant D90
699 indicate reduced river load inputs compared to the previous and following periods, suggesting a reduced
700 river discharge intensity during the wet season. Such weak river discharge is in accordance with the
701 lowest level recorded for Lake Afambo, the drying of Gemeri Lake (Fig. 6a.4) and high evaporative
702 processes of lake waters (Sr peaks), especially between 1991 and 1997, highlighting the occurrence of
703 the most severe drought period that has been recorded over the last ~50 years in the Central Afar Region.
704 During this period, Lake Gemeri dried up, evident in satellite image analyses and in the GEM18-03/-

705 04B lithology characterized by the development of a concomitant pedogenic horizon. During this time
706 the lake Gemeru was occupied by vegetation and incipient soil formation.

707 Between 1998 and 2010, constant Ti/Sr and increase of F1 thickness proxies indicate a gradual increase
708 in river terrigenous inputs in relation to weak dry season drought intensities, except for two years of dry
709 season droughts recorded in 2009 and 2010. The high variable D90 suggests the alternation between
710 yearly high- and low-energy inflow, highlighting a year-by-year hydrological instability of the Awash
711 River catchment for this period.

712 Since the 2010 wet season, the AFA18-02 sequence records a disproportionate increase in sedimentation
713 rate (Fig. 6a.3) and in yearly solid load volume inputs (F1 thickness Fig. 9b), in concomitance with a
714 reduced river energy discharge (low and constant D90) and an average lake water surface decrease of
715 ~100 km² compared to the previous decade (~~Fig. 6~~). Such a hydro-sedimentary anomaly could be
716 attributable to a strong anthropogenic impact such as that induced by the construction of the Tendaho
717 Dam and the related Tendaho reservoir (Dereje et al., 2018; Yemane, 2008). Indeed, between 2010 and
718 2014, the dam project included the reorganization of the hydrographic network of the Lower Awash
719 plain with the massive development of irrigation channels, sugarcane cultivation and a sugar factory
720 (corresponding to the alluvial plain area in Fig. ~~1B1b~~). The increase in solid load discharge could thus
721 be linked to the disproportionate intensification of local soil erosion induced by artificial channel
722 digging and agricultural exploitation of the lower Awash plain. Accordingly, the reduced river flow
723 energy and lake surfaces are related to the water retention of the artificial Tendaho reservoir at the mouth
724 of the Lower Awash plain. For this period, our geochemical and sedimentological data are not discussed
725 in terms of regional climate-induced drought and flood intensities because they are partially
726 disconnected from the regional hydrological dynamics of the Awash River catchment.

727



728
 729 **Figure 9:** Fifty years of Awash seasonal flood/drought magnitudes and their connection with ENSO events recorded in the
 730 AFA18-02 sequence: a) Log(Ti/Sr) XRF ratio; b) F1 thickness; c) D90; d) water flow rate at Tendaho (mm, GR2M); e) SST
 731 temperature anomalies (NOAA, El Niño 3.4) with indicated annual F2 laminae (dry season, yellow lines), enhanced dry
 732 interannual events (red lines) and enhanced wet season/river flood periods (blue lines).

733 **5.3 5.5 Magnitudes of the Awash River wet/drought seasons seasonality, and their connection-comparison with the impacts of ENSO impacts in Horn of Africa events**

734
 735
 736 **Between March and August across Eastern Africa, the monsoonal rainy season is vital for agricultural production and thus for national food security, especially in more susceptible areas such as along the Rift Valley and over distal lowlands. During the last ~50 years, recurrent anomalous low and reduced rainy seasons have had substantial environmental, humanitarian and economic impacts, including agriculture and ecosystem sustainability (Palmer et al., 2023). Recent studies have highlighted how the post-1960s period is characterized by global enhanced ENSO SST variability and magnitude related to anthropogenic activities (rising CO₂ atmospheric concentrations and decreased sulfur aerosols; Cai et al., 2023; Grothe et al., 2020). Post-1960 periods are thus marked by global increased variability features evident in more frequent occurrences of strong El Niño and strong La Niña events (Cai et al., 2023). In Ethiopia, the coincidence of enhanced ENSO episodes and droughts was recorded in 1965, 1972–73, 1982–83, 1986, 1991–93, 1997–98 and 2015–16 (Comenetz and Caviedes, 2002; Mera, 2018). In the Horn of Africa, rainfall anomalies of –100–250 mm year⁻¹ were documented in 1997, 2006, 2012, 2015**

Mis en forme : Retrait : Gauche : 0,25 cm, Sans numérotation ni puces

748 and 2019 and are associated with ENSO and IOD variability and socioeconomic crises (Nicholson,
749 2017; Palmer et al., 2023; Spencer et al., 2005; Webster et al., 1999). Today (until December 2023),
750 ~22 million people are expected to confront acute food insecurity similar to the El Niño induced
751 drought affected areas of Djibouti, Ethiopia, Kenya and Somalia, and will face what is estimated to be
752 the worst drought of the last 40 years (FAO, 2023, 2022).
753 Together with reduced anomalous precipitation during long rainy seasons, subsequent disproportionate
754 short flood events were often recorded, and affected crop production as well as increasing the number
755 of tropical disease outbreaks. For example, during the 1958/59 El Niño event, abnormally high
756 temperature, floods, and relative humidity resulted in 3 million malaria cases across the Ethiopian
757 highlands (Fontaine et al., 1961). During the El Niño of 1997–1998, exceptionally short heavy rains and
758 floods affected food production and distribution networks throughout Eastern Africa. The floods caused
759 extensive damage to crops, losses of large numbers of livestock and an increased incidence of cholera,
760 malaria and rift valley fever linked to the lack of potable water in flooded areas (Palmer et al., 2023).
761 The repetition of such events continues today as recorded in 2022, during which the meagre rainy season
762 was followed by prolonged floods (OCHA, 2022).
763 In order to expand our knowledge base and mitigate difficulties with regards to future adaptation to such
764 extreme changes, it is pivotal to fully understand not only Eastern African seasonal rainfall dynamics,
765 but also regional to local hydraulic system feedbacks to ENSO flood and drought events.
766 East African atmospheric climate modes may operate concurrently between the Indian Ocean Dipole
767 (IOD), South Atlantic SST and ENSO, making it difficult to understand the origin, magnitude and
768 temporal variability of extreme droughts or flooding events (Emerton et al., 2017; Fiechi et al., 2021).
769 Generally, the link between ENSO and IOD anomalies appears to be underestimated in model
770 predictions for East African rainfall during strong El Niño periods (MacLeod and Caminade, 2019).
771 Recent simulation studies have shown that it is difficult to estimate ENSO induced flood and drought
772 hazards in Sub-Saharan Africa as there are significant regional differences which are not sufficiently
773 studied. Indeed, the Main Ethiopian Rift and the Awash River catchment areas are underrepresented in
774 ENSO and IOD climate teleconnection models (Fiechi et al., 2021), reinforcing the importance of our
775 data in the framework of current climatic anomaly studies.
776 The comparison between our wet/dry season intensity reconstruction, the flow rate modelling of the
777 Awash River at Tendaho Lake, and the SST anomalies of the NOAA El Niño model allow us to discuss
778 the high-resolution seasonal hydro-climate variability of the Awash River catchment in relation to El
779 Niño atmospheric anomalies (Fig. 9).
780 We have observed a generally stronger drought in our record during El Niño years, which are known to
781 be associated with low discharge, while La Niña years correspond with relatively high discharge (Abteu
782 et al., 2009; Amarasekera et al., 1997; Camberlin et al., 2001; De Putter et al., 1998; Eltahir, 1996; Wang
783 and Eltahir, 1999; Zaroug et al., 2014; Fig. 9). We have also observed that the occurrence of extreme
784 wet season conditions at the onset of La Niña periods seems proportional to the gradient amplitude

785 between positive and negative ENSO SST temperature anomalies, as is evident in 1998 (Fig. 9).
786 Accordingly, the D90 variability of the AFA18-02 core indicates the occurrence of high hydrological
787 activity during 1975, 1978, 1981/82, 1988/89 years following El Niño-induced droughts documented in
788 1975/76, 1978/79, 1982 and 1987/88 in Ethiopia (Mera, 2018). Overall, along the Afambo sequence, all
789 major El Niño-induced droughts are systematically well recorded by our proxy of drought intensity (red
790 lines Fig. 9; Mera, 2018).

791 High evaporation processes and low fluvial solid load inputs recorded in the AFA18-02 sequence
792 suggest that along the Lower Awash valley, the period between 1991 and 1997 experienced the most
793 extreme and continuous drought in the region of the last ~50 years (Fig. 9). In the Lake Abhe basin,
794 such an event caused the complete drying of Lake Gemeri and a substantial lowering of Lake Afambo
795 (Fig. 6b), suggesting loss of water capacity of the lower Awash plain agricultural fields. In East Africa,
796 the 1997/1998 El Niño tended to have significant socio-economic and health impacts on populations
797 even if it was not as extreme or as widespread as that of 1984 (Palmer et al., 2023). In contrast, the
798 sedimentary record of the Afar lakes has revealed that the 1997 drought was more intense than the 1984
799 drought. Such discrepancy can be attributable to strong regional variability, with particularly arid areas
800 such as the Afar region being more impacted by drought than other East African regions. Accordingly,
801 *United Nations Emergencies Unit for Ethiopia* reports highlight how the 1997 drought was particularly
802 virulent in the Somali Regional state and the Afar, located in the southeast of the Horn of Africa (Borton,
803 1997). As a result of low rains in 1996 and 1997, more than 275,000 people in the Afar Regional State
804 were reported to be affected by drought.

805 At the scale of the Horn of Africa, 1997 is considered to have had socioeconomic impacts principally
806 related to the La Niña flooding events. From October to December 1997, exceptionally heavy rains
807 seriously affected food production throughout Eastern Africa (CARE, 1998; Nicholson, 2017).

808 Accordingly, immediately after the extreme ~~extended drought of the~~ extended drought between 1991 and 1997-dry season,
809 we observe a disproportionate increase in Awash River solid load inputs that were concomitant with La
810 Niña (Fig. 9).

811 From April 2016 to December 2017, the southeastern regions of the Horn of Africa experienced the
812 strongest drought of the last ~40 years which have been linked to the El Niño 2015 event (MacLeod and
813 Caminade, 2019; Mera, 2018). Even if modulated by the Tendaho dam, we observe three consecutive
814 years of reduced sedimentation rates and unwanted evaporation processes from the Afambo sequence
815 indicating that the lower Awash valley had been impacted by anomalously weak rainy seasons in 2015
816 and 2016. In the nearby Somali region, such events triggered acute food shortages and malnutrition
817 exacerbated by a shortage of potable water that led to disease outbreaks, which affected more than six
818 million people (FSNAU, 2022; WBG, 2018).

819 The AFA18-02 sequence has been shown to be an exceptional record of anomalous hydrological events
820 in the region, but quantitative data for regional to local climate change impacts are still lacking. Indeed,
821 our record provides high-resolution wet season and drought magnitude records, highlighting some

822 similarities and divergences compared to historical and instrumental records, which are necessary for
823 the improvement of Eastern African climate prediction models. Such discrepancy can be attributed to
824 the lack of comprehensive instrumental data for the lower Awash River catchment area. Specifically,
825 the flow rates in Tendaho have been modeled using discontinuous and low-resolution datasets. The
826 simulated streamflows at Tendaho are subject to uncertainties arising from several factors: the rainfall-
827 runoff model itself, the calibration of its parameters based on limited observed streamflow data
828 (available only for the period 1990-2014), and the uncertainties in the meteorological inputs (sourced
829 from the NOAA 20CR global reanalysis). This data merits integration into models to test different
830 external forcings and large-scale climate teleconnections and feedbacks (vegetation, dust concentration,
831 ~~IOD~~Indian Ocean Dipole, South Atlantic SST, relationship between ENSO and summer monsoon
832 variability), which have affected inter-annual to multi-centennial hydrological variability in East Africa.

833 **6 Conclusion**

834 In this study, we have demonstrated that the hydro-sedimentary patterns of Central Afar Lakes
835 (Ethiopia) are highly sensitive to changes in yearly precipitation over the Awash River catchment. Using
836 a solid age model, sedimentological and geochemical proxies and microscopic observation on two
837 lacustrine cores cross-referenced with a lake surface reconstruction model from satellite images and
838 seismic imagery, we provide a high-resolution seasonal record of Awash River wet seasons/droughts
839 covering the last ~50 years. Atmospheric anomalies linked to ENSO SST variability are the main factors
840 determining hydrological instability over the Central Afar basin during the last fifty years in terms of
841 flood hazards and drought periods. Between 1969 and 1989, our record shows increased wet season
842 flood activity of the Awash River linked to La Niña, with a moderate impact of the 1984 El Niño on
843 evaporative conditions in the Lake Abhe basin. Between 1991 and 1997, we highlight the occurrence of
844 the strongest prolonged drought ever recorded in the Central Afar Lake region, and demonstrate
845 similarities and divergences between our data and instrumental and historical drought records. This
846 study provides new unpublished data on the impact of ENSO in the region and confirms the utility of
847 this unique quantitative record for the improvement of future regional climate predictions. From a local
848 perspective, we provide robust evidence to demonstrate how the construction of the Tendaho dam along
849 the Awash River associated with extensive agricultural management, strongly affected the
850 hydrosedimentary balance of the Lower Awash Valley from 2010, likely resulting in a disproportionate
851 increase in local soil erodibility along the alluvial plain.

852 The reactivity of local to regional hydrology and soil to global changes remains understated in East
853 African climatic models. This paper demonstrates the importance of studies on regional hydro-system
854 feedbacks to global atmospheric anomalies, to better understand and mitigate the sometimes catastrophic
855 effects of global warming in extreme environments such as the Afar, especially in the context of current
856 climate-induced food insecurity in East Africa (2022-2023 season) and dire predictions for what is
857 ahead.

858

859 **Code and Data availability**

860 The detailed core location and coring information are available on the Cyber Carothèque Nationale of
861 CNRS (<https://cybercarotheque.fr/>). All analytical data presented in this manuscript are available in the
862 Supplementary Material document.

863

864

865 **Author contribution**

866 **C. Mogni:** Conceptualization, Data curation, Formal analysis, Investigation, Supervision, Validation,
867 Visualization, Writing – original draft preparation - review and editing.

868 **M. Revel:** Conceptualization, Funding acquisition, Investigation, Project administration,
869 Supervision, Writing – original draft preparation– review & editing.

870 **E. Chaumillon:** Conceptualization, Investigation, Formal analysis, Data curation, Visualization,
871 Writing– original draft preparation – review & editing.

872 **E. Malet:** Formal analysis, Investigation, Methodology, Resources.

873 **T. Coulombier:** Formal analysis, Investigation, Methodology, Resources.

874 **P. Sabatier:** Conceptualization, Data curation, Formal analysis, Investigation, Resources,
875 Visualization, Writing– original draft preparation – review & editing.

876 **P. Brigode:** Conceptualization, Data curation, Formal analysis, Investigation, Writing– original draft
877 preparation – review & editing.

878 **G. Hervé:** Conceptualization, Data curation, Formal analysis, Investigation, Visualization, Writing –
879 original draft preparation – review & editing.

880 **A.-L. Develle:** Data curation, Formal analysis, Investigation, Methodology, Resources.

881 **L. Schenini:** Data curation, Formal analysis, Investigation.

882 **M. Messous:** Data curation, Formal analysis, Investigation, Methodology, Resources.

883 **G. Davtian:** Data curation, Formal analysis, Investigation, Methodology, Resources.

884 **A. Carré:** Formal analysis, Investigation, Methodology, Resources.

885 **D. Bosch:** Formal analysis, Methodology, Resources.

886 **N. Volto:** Conceptualization, Data curation, Formal analysis, Investigation, Writing – original draft
887 preparation – review & editing.

888 **C. Méndard:** Project administration, Resources.

889 **L. Khalidi:** Conceptualization, Funding acquisition, Project administration, Supervision, Writing -
890 review & editing.

891 **F. Arnaud:** Conceptualization, Investigation, Project administration, Data curation, Supervision,
892 Ressources, Writing – original draft preparation– review & editing.

893

894 **Competing Interests**

895 The authors declare that they have no conflict of interest

896

897 **Acknowledgements**

898 The CLIMAFAR (PIs: L. Khalidi & M. Revel) December 2018 coring operations were carried
899 out in the framework of the VAPOR-Afar project (PI: L. Khalidi) with a permit granted by the
900 Ethiopian Authority for Research and Conservation of Cultural Heritage (ARCCH, Addis
901 Ababa, Ethiopia) in collaboration with the Afar Bureau of Tourism & Culture. Funding for
902 CLIMAFAR was granted by the French government, and managed by the Agence Nationale de
903 la Recherche under the Investissements d'Avenir UCAJEDI project, reference no. ANR-15-
904 IDEX-01 . XRF-Core Scanner and thin section fabrication were performed at the EDYTEM
905 laboratory with funding from the CLIMAFAR grant. XRD analyses were funded by a
906 University Cote d'Azur doctoral grant (C. Mogni). Radiocarbon dating was performed with
907 funding from an ARTEMIS grant and support from the Geoazur laboratory (M. Revel) using
908 the MICHADAS facilities (Christine Hatté; LSCE – UMR 8212 CEA-CNRS-UVSQ). The authors
909 thank the Laboratoire Souterrain de Modane (LSM) facilities for the gamma spectrometry
910 measurements and Environnement, Dynamique et Territoires de Montagne (EDyTeM) for the
911 X-ray fluorescence analyses (A.-L. Develle). We would like to thank the Ethiopian ARCCH,
912 the Afar Bureau of Tourism & Culture and the French Center for Ethiopian Studies (CFEE) for
913 their authorization and support with regards to fieldwork and logistics. We also thank Dr.
914 Tatiana Theodoropoulou and Dr. Lucie Coudert for the fish species determination of the
915 AFA18-02 core sequence.

916

917 **References**

- 918 Abtew, W., Melesse, A.M., Dessalegne, T., 2009. El Niño Southern Oscillation link to the Blue
919 Nile River Basin hydrology. *Hydrological Processes* 23, 3653–3660.
920 <https://doi.org/10.1002/hyp.7367>
- 921 Amarasekera, K.N., Lee, R.F., Williams, E.R., Eltahir, E.A.B., 1997. ENSO and the natural
922 variability in the flow of tropical rivers. *Journal of Hydrology* 200, 24–39.
923 [https://doi.org/10.1016/S0022-1694\(96\)03340-9](https://doi.org/10.1016/S0022-1694(96)03340-9)
- 924 Arnaud, F., Poulenard, J., Giguët-Covex, C., Wilhelm, B., Révillon, S., Jenny, J.-P., Revel, M.,
925 Enters, D., Bajard, M., Fouinat, L., Doyen, E., Simonneau, A., Pignol, C., Chapron, E.,
926 Vannière, B., Sabatier, P., 2016. Erosion under climate and human pressures: An
927 alpine lake sediment perspective. *Quaternary Science Reviews* 152, 1–18.
928 <https://doi.org/10.1016/j.quascirev.2016.09.018>

Mis en forme : Français (France)

- 929 Arnaud, F., Sabatier, P., 2022. Lakes as Recorders of Earth Surface Dynamics From Yearly to
 930 Plurimillennial Time-Scales, in: Mehner, T., Tockner, K. (Eds.), *Encyclopedia of Inland*
 931 *Waters* (Second Edition). Elsevier, Oxford, pp. 439–452.
 932 <https://doi.org/10.1016/B978-0-12-819166-8.00125-0>
- 933 Arneitz, P., Leonhardt, R., Egli, R., Fabian, K., 2021. Dipole and Nondipole Evolution of the
 934 Historical Geomagnetic Field From Instrumental, Archeomagnetic, and Volcanic Data.
 935 *Journal of Geophysical Research: Solid Earth* 126, e2021JB022565.
 936 <https://doi.org/10.1029/2021JB022565>
- 937 Ashley, G.M., 2002. 11 - Glaciolacustrine environments, in: Menzies, J. (Ed.), *Modern and*
 938 *Past Glacial Environments*. Butterworth-Heinemann, Oxford, pp. 335–359.
 939 <https://doi.org/10.1016/B978-075064226-2/50014-3>
- 940 Ayalew, D., Jung, S., Romer, R.L., Kersten, F., Pfänder, J.A., Garbe-Schönberg, D., 2016.
 941 Petrogenesis and origin of modern Ethiopian rift basalts: Constraints from isotope
 942 and trace element geochemistry. *Lithos* 258–259, 1–14.
 943 <https://doi.org/10.1016/j.lithos.2016.04.001>
- 944 Bajard, M., Poulénard, J., Sabatier, P., Develle, A.-L., Giguët-Covex, C., Jacob, J., Crouzet, C.,
 945 David, F., Pignol, C., Arnaud, F., 2017. Progressive and regressive soil evolution
 946 phases in the Anthropocene. *CATENA* 150, 39–52.
 947 <https://doi.org/10.1016/j.catena.2016.11.001>
- 948 Bajard, M., Sabatier, P., David, F., Develle, A.-L., Reyss, J.-L., Fanget, B., Malet, E., Arnaud, D.,
 949 Augustin, L., Crouzet, C., Poulénard, J., Arnaud, F., 2016. Erosion record in Lake La
 950 Thuile sediments (Prealps, France): Evidence of montane landscape dynamics
 951 throughout the Holocene. *The Holocene* 26, 350–364.
 952 <https://doi.org/10.1177/0959683615609750>
- 953 Barberi, F., Varet, J., 1977. Volcanism of Afar: Small-scale plate tectonics implications. *Geol.*
 954 *Soc. Am. Bull.*, 88, 1251–1266.
- 955 Bastian, L., Vigier, N., Revel, M., Yirgu, G., Ayalew, D., Pik, R., 2019. Chemical erosion rates in
 956 the upper Blue Nile Basin and related atmospheric CO₂ consumption. *Chemical*
 957 *Geology* 518, 19–31. <https://doi.org/10.1016/j.chemgeo.2019.03.033>
- 958 Bates, C.C., 1953. RATIONAL THEORY OF DELTA FORMATION1. *AAPG Bulletin* 37, 2119–2162.
 959 <https://doi.org/10.1306/5CEADD76-16BB-11D7-8645000102C1865D>
- 960 Beck, H.E., Wood, E.F., Pan, M., Fisher, C.K., Miralles, D.G., Dijk, A.I.J.M. van, McVicar, T.R.,
 961 Adler, R.F., 2019. MSWEP V2 Global 3-Hourly 0.1° Precipitation: Methodology and
 962 Quantitative Assessment. *Bulletin of the American Meteorological Society* 100, 473–
 963 500. <https://doi.org/10.1175/BAMS-D-17-0138.1>
- 964 Bertin, X., Chaumillon, E., 2005. New Insights in Shallow Gas Generation from Very High
 965 Resolution Seismic and Bathymetric Surveys in the Marennes-Oléron Bay, France.
 966 *Mar Geophys Res* 26, 225–233. <https://doi.org/10.1007/s11001-005-3720-y>
- 967 Borton, J., 1997. Ethiopia Monthly Information Report Apr 1997. United Nations
 968 Emergencies Unit for Ethiopia (UN-EUE).
- 969 Borton, J., 7. Ethiopia Monthly Information Report March 1997. United Nations Emergencies
 970 Unit for Ethiopia.
- 971 Brown, M.C., Hervé, G., Korte, M., Genevey, A., 2021. Global archaeomagnetic data: The
 972 state of the art and future challenges. *Physics of the Earth and Planetary Interiors*
 973 318, 106766. <https://doi.org/10.1016/j.pepi.2021.106766>

Mis en forme : Français (France)

Mis en forme : Français (France)

- 974 Bruel, R., Sabatier, P., 2020. serac: an R package for Shortlived RADionuclide chronology of
 975 recent sediment cores. *Journal of Environmental Radioactivity* 225, 106449.
 976 <https://doi.org/10.1016/j.jenvrad.2020.106449>
- 977 Cai, W., Ng, B., Geng, T., Jia, F., Wu, L., Wang, G., Liu, Yu, Gan, B., Yang, K., Santoso, A., Lin,
 978 X., Li, Z., Liu, Yi, Yang, Y., Jin, F.-F., Collins, M., McPhaden, M.J., 2023. Anthropogenic
 979 impacts on twentieth-century ENSO variability changes. *Nat Rev Earth Environ* 1–12.
 980 <https://doi.org/10.1038/s43017-023-00427-8>
- 981 Camberlin, P., Janicot, S., Pocard, I., 2001. Seasonality and atmospheric dynamics of the
 982 teleconnection between African rainfall and tropical sea-surface temperature:
 983 Atlantic vs. ENSO. *International Journal of Climatology* 21, 973–1005.
 984 <https://doi.org/10.1002/joc.673>
- 985 Campbell, C., 1998. Late Holocene Lake Sedimentology and Climate Change in Southern
 986 Alberta, Canada. *Quaternary Research* 49, 96–101.
 987 <https://doi.org/10.1006/qres.1997.1946>
- 988 Campos, H., Steffen, W., Aguero, G., Parra, O., Zuniga, L., 1989. Estudios limnológicos en el
 989 Lago Puyehue (Chile) : morfometria, factores físicos y químicos, plancton y
 990 productividad primaria. *Medio ambiente (Valdivia)* 10, 36–53.
- 991 Campuzano, S.A., Gómez-Paccard, M., Pavón-Carrasco, F.J., Osete, M.L., 2019. Emergence
 992 and evolution of the South Atlantic Anomaly revealed by the new paleomagnetic
 993 reconstruction SHAWQ2k. *Earth and Planetary Science Letters* 512, 17–26.
 994 <https://doi.org/10.1016/j.epsl.2019.01.050>
- 995 CARE, 1998. El Niño in 1997-1998: Impacts and CARE's Response.
- 996 Chapron, E., Ariztegui, D., Mulsow, S., Villarosa, G., Pino, M., Outes, V., Juvigné, E., Crivelli,
 997 E., 2006. Impact of the 1960 major subduction earthquake in Northern Patagonia
 998 (Chile, Argentina). *Quaternary International, Holocene environmental catastrophes in*
 999 *South America: from the lowlands to the Andes* 158, 58–71.
 1000 <https://doi.org/10.1016/j.quaint.2006.05.017>
- 1001 Chapron, E., Juvigné, E., Mulsow, S., Ariztegui, D., Magand, O., Bertrand, S., Pino, M.,
 1002 Chapron, O., 2007. Recent clastic sedimentation processes in Lake Puyehue (Chilean
 1003 Lake District, 40.5°S). *Sedimentary Geology* 201, 365–385.
 1004 <https://doi.org/10.1016/j.sedgeo.2007.07.006>
- 1005 Cohen, A.S., 2003. *Paleolimnology: The History and Evolution of Lake Systems*. Oxford
 1006 University Press.
- 1007 Comenetz, J., Caviedes, C., 2002. Climate variability, political crises, and historical population
 1008 displacements in Ethiopia. *Global Environmental Change Part B: Environmental*
 1009 *Hazards* 4, 113–127. <https://doi.org/10.1016/j.hazards.2003.08.001>
- 1010 Coron, L., Delaigue, O., Thirel, G., Dorchie, D., Perrin, C., Michel, C., 2022. airGR: Suite of GR
 1011 Hydrological Models for Precipitation-Runoff Modelling (v. 1.7.0). airGR.
- 1012 Coron, L., Thirel, G., Delaigue, O., Perrin, C., Andréassian, V., 2017. The suite of lumped GR
 1013 hydrological models in an R package. *Environmental Modelling & Software* 94, 166–
 1014 171. <https://doi.org/10.1016/j.envsoft.2017.05.002>
- 1015 Croudace, I.W., Rothwell, R.G. (Eds.), 2015. *Micro-XRF Studies of Sediment Cores,*
 1016 *Developments in Paleoenvironmental Research*. Springer Netherlands, Dordrecht.
 1017 <https://doi.org/10.1007/978-94-017-9849-5>
- 1018 Crouzet, C., Wilhelm, B., Sabatier, P., Demory, F., Thouveny, N., Pignol, C., Reyss, J.-L.,
 1019 Magand, O., Jeltsch-Thömmes, A., Bajard, M., Augustin, L., Arnaud, F., 2019.

Mis en forme : Français (France)

Mis en forme : Italien (Italie)

1020 Palaeomagnetism for chronologies of recent alpine lake sediments: successes and
1021 limits. *J Paleolimnol* 62, 259–278. <https://doi.org/10.1007/s10933-019-00087-z>

1022 De Putter, T., Loutre, M.-F., Wansard, G., 1998. Decadal periodicities of Nile River historical
1023 discharge (A.D. 622–1470) and climatic implications. *Geophysical Research Letters*
1024 25, 3193–3196. <https://doi.org/10.1029/98GL02250>

1025 Dereje, H., Daneal, S.F., Yenesew, M., Azage, G.Y., Tadesse, S., Naod, M., Tariku, A., 2018.
1026 The Study of Water Use and Treated Wastewater Discharge charge. Report on Charge
1027 System for Irrigation Water Abstraction and Use. Federal Democratic Republic of
1028 Ethiopia Awash Basin Authority.

1029 Dosio, A., Jones, R.G., Jack, C., Lennard, C., Nikulin, G., Hewitson, B., 2019. What can we
1030 know about future precipitation in Africa? Robustness, significance and added value
1031 of projections from a large ensemble of regional climate models. *Clim Dyn* 53, 5833–
1032 5858. <https://doi.org/10.1007/s00382-019-04900-3>

1033 Eltahir, E.A.B., 1996. El Niño and the Natural Variability in the Flow of the Nile River. *Water*
1034 *Resour. Res.* 32, 131–137. <https://doi.org/10.1029/95WR02968>

1035 Emerton, R., Cloke, H.L., Stephens, E.M., Zsoter, E., Woolnough, S.J., Pappenberger, F., 2017.
1036 Complex picture for likelihood of ENSO-driven flood hazard. *Nat Commun* 8, 14796.
1037 <https://doi.org/10.1038/ncomms14796>

1038 FAO, 2023. Drought in the Horn of Africa: Progress report on the rapid response and
1039 mitigation plan to avert a humanitarian catastrophe (January–December 2022). FAO.
1040 <https://doi.org/10.4060/cc4218en>

1041 FAO, 2022. Drought in the Horn of Africa – Rapid response and mitigation plan to avert a
1042 humanitarian catastrophe. FAO. <https://doi.org/10.4060/cb8280en>

1043 FAO, 2000. The Elimination of Food Insecurity in the Horn of Africa – Summary Report.
1044 Rome.

1045 Ficchi, A., Cloke, H., Neves, C., Woolnough, S., Coughlan de Perez, E., Zsoter, E., Pinto, I.,
1046 Meque, A., Stephens, E., 2021. Beyond El Niño: Unsung climate modes drive African
1047 floods. *Weather and Climate Extremes* 33, 100345.
1048 <https://doi.org/10.1016/j.wace.2021.100345>

1049 Folk, R.L., Ward, W.C., 1957. Brazos River Bar: A Study in the Significance of Grain Size
1050 Parameters. *Journal Of Sedimentary Petrology* 27, 3–26.

1051 Fontaine, R.E., Najjar, A.E., Prince, J.S., 1961. The 1958 malaria epidemic in Ethiopia. *Am J*
1052 *Trop Med Hyg* 10, 795–803. <https://doi.org/10.4269/ajtmh.1961.10.795>

1053 Foucher, A., Chaboche, P.-A., Sabatier, P., Evrard, O., 2021. A worldwide meta-analysis
1054 (1977–2020) of sediment core dating using fallout radionuclides including ¹³⁷Cs and
1055 ²¹⁰Pb_{xs}. *Earth System Science Data* 13, 4951–4966. <https://doi.org/10.5194/essd-13-4951-2021>

1057 FSNAU, 2022. Somalia FSNAU Food Security & Nutrition Quarterly Brief — Focus on Post Gu
1058 2017 Season Early Warning (Food Security and Nutrition Analysis Unit and Famine
1059 Early Warning System Network, 2022). FSNAU.

1060 Garcia-Gil, S., Vilas, F., Garcia-Garcia, A., 2002. Shallow gas features in incised-valley fills (Ría
1061 de Vigo, NW Spain): a case study. *Continental Shelf Research* 22, 2303–2315.
1062 [https://doi.org/10.1016/S0278-4343\(02\)00057-2](https://doi.org/10.1016/S0278-4343(02)00057-2)

1063 Gilli, A., Anselmetti, F.S., Glur, L., Wirth, S.B., 2013. Lake Sediments as Archives of
1064 Recurrence Rates and Intensities of Past Flood Events, in: Schneuwly-Bollschweiler,
1065 M., Stoffel, M., Rudolf-Miklau, F. (Eds.), *Dating Torrential Processes on Fans and*
1066 *Cones: Methods and Their Application for Hazard and Risk Assessment, Advances in*

1067 Global Change Research. Springer Netherlands, Dordrecht, pp. 225–242.
 1068 https://doi.org/10.1007/978-94-007-4336-6_15

1069 Grothe, P.R., Cobb, K.M., Liguori, G., Di Lorenzo, E., Capotondi, A., Lu, Y., Cheng, H., Edwards,
 1070 R.L., Southon, J.R., Santos, G.M., Deocampo, D.M., Lynch-Stieglitz, J., Chen, T., Sayani,
 1071 H.R., Thompson, D.M., Conroy, J.L., Moore, A.L., Townsend, K., Hagos, M., O'Connor,
 1072 G., Toth, L.T., 2020. Enhanced El Niño–Southern Oscillation Variability in Recent
 1073 Decades. *Geophysical Research Letters* 47, e2019GL083906.
 1074 <https://doi.org/10.1029/2019GL083906>

1075 Haberzettl, T., Kirsten, K.L., Kasper, T., Franz, S., Reinwarth, B., Baade, J., Daut, G., Meadows,
 1076 M.E., Su, Y., Mäusbacher, R., 2019. Using 210Pb-data and paleomagnetic secular
 1077 variations to date anthropogenic impact on a lake system in the Western Cape, South
 1078 Africa. *Quaternary Geochronology* 51, 53–63.
 1079 <https://doi.org/10.1016/j.quageo.2018.12.004>

1080 Hersbach, H., Bell, B., Berrisford, P., Hirahara, S., Horányi, A., Muñoz-Sabater, J., Nicolas, J.,
 1081 Peubey, C., Radu, R., Schepers, D., Simmons, A., Soci, C., Abdalla, S., Abellan, X.,
 1082 Balsamo, G., Bechtold, P., Biavati, G., Bidlot, J., Bonavita, M., De Chiara, G., Dahlgren,
 1083 P., Dee, D., Diamantakis, M., Dragani, R., Flemming, J., Forbes, R., Fuentes, M., Geer,
 1084 A., Haimberger, L., Healy, S., Hogan, R.J., Hólm, E., Janisková, M., Keeley, S., Laloyaux,
 1085 P., Lopez, P., Lupu, C., Radnoti, G., de Rosnay, P., Rozum, I., Vamborg, F., Villaume, S.,
 1086 Thépaut, J.-N., 2020. The ERA5 global reanalysis. *Quarterly Journal of the Royal
 1087 Meteorological Society* 146, 1999–2049. <https://doi.org/10.1002/qj.3803>

1088 Hua, Q., Barbetti, M., Rakowski, A.Z., 2013. Atmospheric radiocarbon for the period 1950-
 1089 2010.

1090 IPCC, 2022. Working Group II contribution to the Sixth Assessment Report of the
 1091 Intergovernmental Panel on Climate Change.

1092 Jackson, A., Jonkers, A.R.T., Walker, M.R., 2000. Four Centuries of Geomagnetic Secular
 1093 Variation from Historical Records. *Philosophical Transactions: Mathematical, Physical
 1094 and Engineering Sciences* 358, 957–990.

1095 Jackson, M.L., 2005. Soil chemical analysis : advanced course : a manual of methods useful
 1096 for instruction and research in soil chemistry, physical chemistry of soils, soil fertility,
 1097 and soil genesis. Parallel Press, University of Wisconsin-Madison Libraries, [2005]
 1098 ©2005, Revised second edition. Madison, Wis.

1099 Jenny, J.-P., Wilhelm, B., Arnaud, F., Sabatier, P., Giguet Covex, C., Mélo, A., Fanget, B.,
 1100 Malet, E., Ployon, E., Perga, M.E., 2014. A 4D sedimentological approach to
 1101 reconstructing the flood frequency and intensity of the Rhône River (Lake Bourget,
 1102 NW European Alps). *J Paleolimnol* 51, 469–483. <https://doi.org/10.1007/s10933-014-9768-4>

1103 Kidane, D., Mekonnen, A., Teketay, D., 2014. Contributions of Tendaho Irrigation Project to
 1104 the Improvement of Livelihoods of Agropastoralists in the Lower Awash Basin,
 1105 Northeastern Ethiopia. *Ethiopian e-journal for research and innovation foresight* 6, 1–
 1106 19.

1107
 1108 Kylander, M.E., Ampel, L., Wohlfarth, B., Veres, D., 2011. High-resolution X-ray fluorescence
 1109 core scanning analysis of Les Echets (France) sedimentary sequence: new insights
 1110 from chemical proxies. *Journal of Quaternary Science* 26, 109–117.
 1111 <https://doi.org/10.1002/jqs.1438>

Mis en forme : Italien (Italie)

- 1112 Lapointe, F., Francus, P., Lamoureux, S.F., Saïd, M., Cuven, S., 2012. 1750 years of large
 1113 rainfall events inferred from particle size at East Lake, Cape Bounty, Melville Island,
 1114 Canada. *J Paleolimnol* 48, 159–173. <https://doi.org/10.1007/s10933-012-9611-8>
- 1115 Lefebvre, P., Sabatier, P., Mangeret, A., Gourgiotis, A., Le Pape, P., Develle, A.-L., Louvat, P.,
 1116 Diez, O., Reyss, J.-L., Gaillardet, J., Cazala, C., Morin, G., 2021. Climate-driven fluxes of
 1117 organic-bound uranium to an alpine lake over the Holocene. *Science of The Total*
 1118 *Environment* 783, 146878. <https://doi.org/10.1016/j.scitotenv.2021.146878>
- 1119 Lennard, C.J., Nikulin, G., Dosio, A., Moufouma-Okia, W., 2018. On the need for regional
 1120 climate information over Africa under varying levels of global warming. *Environ. Res.*
 1121 *Lett.* 13, 060401. <https://doi.org/10.1088/1748-9326/aab2b4>
- 1122 Li, C.-G., Zheng, Y., Wang, M., Sun, Z., Jin, C., Hou, J., 2021. Refined dating using
 1123 palaeomagnetic secular variations on a lake sediment core from Guozha Co,
 1124 northwestern Tibetan Plateau. *Quaternary Geochronology* 62, 101146.
 1125 <https://doi.org/10.1016/j.quageo.2020.101146>
- 1126 MacLeod, D., Caminade, C., 2019. The Moderate Impact of the 2015 El Niño over East Africa
 1127 and Its Representation in Seasonal Reforecasts. *Journal of Climate* 32, 7989–8001.
 1128 <https://doi.org/10.1175/JCLI-D-19-0201.1>
- 1129 Martín-Puertas, C., Valero-Garcés, B.L., Mata, M.P., Moreno, A., Giral, S., Martínez-Ruiz, F.,
 1130 Jiménez-Espejo, F., 2011. Geochemical processes in a Mediterranean Lake: a high-
 1131 resolution study of the last 4,000 years in Zoñar Lake, southern Spain. *Journal of*
 1132 *Paleolimnology* 46, 405–421. <https://doi.org/10.1007/s10933-009-9373-0>
- 1133 Marzin, C., Braconnot, P., 2009. The role of the ocean feedback on Asian and African
 1134 monsoon variations at 6kyr and 9.5kyr BP. *Comptes Rendus Geoscience* 341, 643–
 1135 655. <https://doi.org/10.1016/j.crte.2009.09.001>
- 1136 Mera, G.A., 2018. Drought and its impacts in Ethiopia. *Weather and Climate Extremes* 22,
 1137 24–35. <https://doi.org/10.1016/j.wace.2018.10.002>
- 1138 Molinaroli, E., Guerzoni, S., De Falco, G., Sarretta, A., Cucco, A., Como, S., Simeone, S., Perilli,
 1139 A., Magni, P., 2009. Relationships between hydrodynamic parameters and grain size
 1140 in two contrasting transitional environments: The Lagoons of Venice and Cabras,
 1141 Italy. *Sedimentary Geology* 219, 196–207.
 1142 <https://doi.org/10.1016/j.sedgeo.2009.05.013>
- 1143 Mologni, C., Bruxelles, L., Schuster, M., Davtian, G., Ménard, C., Orange, F., Doubre, C.,
 1144 Cauliez, J., Tazaz, H.B., Revel, M., Khalidi, L., 2021. Holocene East African monsoonal
 1145 variations recorded in wave-dominated clastic paleo-shorelines of Lake Abhe, Central
 1146 Afar region (Ethiopia & Djibouti). *Geomorphology* 391, 107896.
 1147 <https://doi.org/10.1016/j.geomorph.2021.107896>
- 1148 Mologni, C., Revel, M., Blanchet, C., Bosch, D., Develle, A.-L., Orange, F., Bastian, L., Khalidi,
 1149 L., Ducassou, E., Migeon, S., 2020. Frequency of exceptional Nile flood events as an
 1150 indicator of Holocene hydro-climatic changes in the Ethiopian Highlands. *Quaternary*
 1151 *Science Reviews* 247, 106543. <https://doi.org/10.1016/j.quascirev.2020.106543>
- 1152 Mouelhi, S., Michel, C., Perrin, C., Andréassian, V., 2006. Stepwise development of a two-
 1153 parameter monthly water balance model. *Journal of Hydrology* 318, 200–214.
 1154 <https://doi.org/10.1016/j.jhydrol.2005.06.014>
- 1155 Murray, H.D., 1975. *Melanoides tuberculata* (Müller), Las Morras Creek, Bracketville.
 1156 *Bulletin Of The American Malacological Union* 1, 43.

Mis en forme : Français (France)

Mis en forme : Français (France)

Mis en forme : Italien (Italie)

- 1157 Nash, J.E., Sutcliffe, J.V., 1970. River flow forecasting through conceptual models part I — A
 1158 discussion of principles. *Journal of Hydrology* 10, 282–290.
 1159 [https://doi.org/10.1016/0022-1694\(70\)90255-6](https://doi.org/10.1016/0022-1694(70)90255-6)
- 1160 Niang, I., Ruppel, O.C., Abd rabo, M.A., Essel, A., Lennard, C., Padgham, J., Urquhart, P.,
 1161 Adelekan, I., Archibald, S., Barkhordarian, A., Battersby, J., Chahed, M., Chatterjee,
 1162 M., Chidzie, C.T., Descheemaeker, K., Djoudi, H., Ebi, K.L., Fall, P.D., Fuentes, R.,
 1163 Garland, R., Harvey, B., Hayden, M., Hemp, A., Jobbins, G., Johnson, J., Lobell, D.,
 1164 Locatelli, B., Ludi, E., Naess, L.O., Ndebele-Murisa, M.R., Ndiaye, A., Newsham, A.,
 1165 Njai, S., Pauw, P., Pramova, E., Rakotondrafara, M.-L., Raleigh, C., Roberts, D.,
 1166 Schleyer, M.H., Victor, D., Vincent, K., Dube, P., Leary, N., Schulte-Uebbing, L., 2014.
 1167 Part B: Regional Aspects. Contribution of Working Group II to the Fifth Assessment
 1168 Report of the Intergovernmental Panel on Climate Change - Africa, in: *Climate*
 1169 *Change 2014: Impacts, Adaptation, and Vulnerability.*, Cambridge University Press.
 1170 Cambridge, United Kingdom and New York, NY, USA, pp. 1199–1265.
- 1171 Nicholson, S.E., 2017. Climate and climatic variability of rainfall over eastern Africa. *Reviews*
 1172 *of Geophysics* 55, 590–635. <https://doi.org/10.1002/2016RG000544>
- 1173 OCHA, 2022. Horn of Africa Drought: Regional Humanitarian Overview & Call to Action.
 1174 OCHA.
- 1175 Ólafsdóttir, S., Geirsdóttir, Á., Miller, G.H., Stoner, J.S., Channell, J.E.T., 2013. Synchronizing
 1176 Holocene lacustrine and marine sediment records using paleomagnetic secular
 1177 variation. *Geology* 41, 535–538. <https://doi.org/10.1130/G33946.1>
- 1178 Oudin, L., Hervieu, F., Michel, C., Perrin, C., Andréassian, V., Anctil, F., Loumagne, C., 2005.
 1179 Which potential evapotranspiration input for a lumped rainfall–runoff model?: Part
 1180 2—Towards a simple and efficient potential evapotranspiration model for rainfall–
 1181 runoff modelling. *Journal of Hydrology* 303, 290–306.
 1182 <https://doi.org/10.1016/j.jhydrol.2004.08.026>
- 1183 Palmer, P.I., Wainwright, C.M., Dong, B., Maidment, R.I., Wheeler, K.G., Gedney, N.,
 1184 Hickman, J.E., Madani, N., Folwell, S.S., Abdo, G., Allan, R.P., Black, E.C.L., Feng, L.,
 1185 Gudoshava, M., Haines, K., Huntingford, C., Kilavi, M., Lunt, M.F., Shaaban, A., Turner,
 1186 A.G., 2023. Drivers and impacts of Eastern African rainfall variability. *Nat Rev Earth*
 1187 *Environ* 4, 254–270. <https://doi.org/10.1038/s43017-023-00397-x>
- 1188 Parris, A.S., Bierman, P.R., Noren, A.J., Prins, M.A., Lini, A., 2010. Holocene paleostorms
 1189 identified by particle size signatures in lake sediments from the northeastern United
 1190 States. *J Paleolimnol* 43, 29–49. <https://doi.org/10.1007/s10933-009-9311-1>
- 1191 Pekel, J.-F., Cottam, A., Gorelick, N., Belward, A.S., 2016. High-resolution mapping of global
 1192 surface water and its long-term changes. *Nature* 540, 418–422.
 1193 <https://doi.org/10.1038/nature20584>
- 1194 Phillips, J.D., 2003. Sources of nonlinearity and complexity in geomorphic systems. *Progress*
 1195 *in Physical Geography: Earth and Environment* 27, 1–23.
 1196 <https://doi.org/10.1191/0309133303pp340ra>
- 1197 Rauch, S., Hemond, H.F., Brabander, D.J., 2006. High spatial resolution analysis of lake
 1198 sediment cores by laser ablation inductively coupled plasma-mass spectrometry (LA-
 1199 ICP-MS): Lake sediment cores by laser ablation-ICP-MS. *Limnol. Oceanogr. Methods*
 1200 4, 268–274. <https://doi.org/10.4319/lom.2006.4.268>
- 1201 Reyss, J.-L., Schmidt, S., Legeleux, F., Bonté, P., 1995. Large, low background well-type
 1202 detectors for measurements of environmental radioactivity. *Nuclear Instruments and*

Mis en forme : Français (France)

- 1203 Methods in Physics Research Section A: Accelerators, Spectrometers, Detectors and
 1204 Associated Equipment 357, 391–397. [https://doi.org/10.1016/0168-9002\(95\)00021-6](https://doi.org/10.1016/0168-9002(95)00021-6)
- 1205 Rousset, E.G., Sauvadet, A.-L., Allard, J., Chaduteau, C., Richard, P., Bonavita, M.-A.C.,
 1206 Chaumillon, E., 2009. Archaeal Methane Cycling Communities Associated with Gassy
 1207 Subsurface Sediments of Marennes-Oléron Bay (France). *Geomicrobiology Journal*
 1208 26, 31–43. <https://doi.org/10.1080/01490450802599284>
- 1209 Sabatier, P., Moernaut, J., Bertrand, S., Van Daele, M., Kremer, K., Chaumillon, E., Arnaud, F.,
 1210 2022. A Review of Event Deposits in Lake Sediments. *Quaternary* 5, 34.
 1211 <https://doi.org/10.3390/quat5030034>
- 1212 Sabatier, P., Wilhelm, B., Ficotola, G.F., Moiroux, F., Poulenard, J., Develle, A.-L., Bichet, A.,
 1213 Chen, W., Pignol, C., Reyss, J.-L., Gielly, L., Bajard, M., Perrette, Y., Malet, E., Taberlet,
 1214 P., Arnaud, F., 2017. 6-kyr record of flood frequency and intensity in the western
 1215 Mediterranean Alps – Interplay of solar and temperature forcing. *Quaternary Science*
 1216 *Reviews* 170, 121–135. <https://doi.org/10.1016/j.quascirev.2017.06.019>
- 1217 Schiefer, E., Gilbert, R., Hassan, M.A., 2011. A lake sediment-based proxy of floods in the
 1218 Rocky Mountain Front Ranges, Canada. *J Paleolimnol* 45, 137–149.
 1219 <https://doi.org/10.1007/s10933-010-9485-6>
- 1220 Slivinski, L.C., Compo, G.P., Whitaker, J.S., Sardeshmukh, P.D., Giese, B.S., McColl, C., Allan,
 1221 R., Yin, X., Vose, R., Titchner, H., Kennedy, J., Spencer, L.J., Ashcroft, L., Brönnimann,
 1222 S., Brunet, M., Camuffo, D., Cornes, R., Cram, T.A., Crouthamel, R., Domínguez-
 1223 Castro, F., Freeman, J.E., Gergis, J., Hawkins, E., Jones, P.D., Jourdain, S., Kaplan, A.,
 1224 Kubota, H., Blancq, F.L., Lee, T.-C., Lorrey, A., Luterbacher, J., Maugeri, M., Mock, C.J.,
 1225 Moore, G.W.K., Przybylak, R., Pudmenzky, C., Reason, C., Slonosky, V.C., Smith, C.A.,
 1226 Tinz, B., Trewin, B., Valente, M.A., Wang, X.L., Wilkinson, C., Wood, K., Wyszyński, P.,
 1227 2019. Towards a more reliable historical reanalysis: Improvements for version 3 of
 1228 the Twentieth Century Reanalysis system. *Quarterly Journal of the Royal*
 1229 *Meteorological Society* 145, 2876–2908. <https://doi.org/10.1002/qj.3598>
- 1230 Spencer, T., Laughton, A.S., Flemming, N.C., Black, E., 2005. The relationship between Indian
 1231 Ocean sea–surface temperature and East African rainfall. *Philosophical Transactions*
 1232 *of the Royal Society A: Mathematical, Physical and Engineering Sciences* 363, 43–47.
 1233 <https://doi.org/10.1098/rsta.2004.1474>
- 1234 Syvitski, J., Ángel, J.R., Saito, Y., Overeem, I., Vörösmarty, C.J., Wang, H., Olago, D., 2022.
 1235 Earth’s sediment cycle during the Anthropocene. *Nat Rev Earth Environ* 3, 179–196.
 1236 <https://doi.org/10.1038/s43017-021-00253-w>
- 1237 Taddese, G., Sonder, K., Peden, D., 2010. THE WATER OF THE AWASH RIVER BASIN A FUTURE
 1238 CHALLENGE TO ETHIOPIA. report 14.
- 1239 Varet, J., 2018. *Geology of Afar (East Africa)*, Springer. ed, *Regional Geology Reviews*.
- 1240 Wang, G., Eltahir, E.A.B., 1999. Use of ENSO Information in Medium- and Long-Range
 1241 Forecasting of the Nile Floods. *Journal of Climate* 12, 1726–1737.
 1242 [https://doi.org/10.1175/1520-0442\(1999\)012<1726:UOEIIM>2.0.CO;2](https://doi.org/10.1175/1520-0442(1999)012<1726:UOEIIM>2.0.CO;2)
- 1243 Ward, P.J., Eisner, S., Flörke, M., Dettinger, M.D., Kummerow, M., 2014. Annual flood
 1244 sensitivities to El Niño–Southern Oscillation at the global scale. *Hydrology and Earth*
 1245 *System Sciences* 18, 47–66. <https://doi.org/10.5194/hess-18-47-2014>
- 1246 WBG, 2018. *Somalia Drought Impact and Needs Assessment: Synthesis Report* (World Bank
 1247 Group, 2018). World Bank Group.

Mis en forme : Français (France)

- 1248 Webster, P.J., Moore, A.M., Loschnigg, J.P., Leben, R.R., 1999. Coupled ocean-atmosphere
1249 dynamics in the Indian Ocean during 1997-98. *Nature* 401, 356–360.
1250 <https://doi.org/10.1038/43848>
- 1251 Weltje, G.J., Tjallingii, R., 2008. Calibration of XRF core scanners for quantitative geochemical
1252 logging of sediment cores: Theory and application. *Earth and Planetary Science*
1253 *Letters* 274, 423–438. <https://doi.org/10.1016/j.epsl.2008.07.054>
- 1254 Wilhelm, B., Arnaud, F., Sabatier, P., Crouzet, C., Brisset, E., Guiter, F., Reyss, J.L., Chaumillon,
1255 E., Tachikawa, K., Bard, E., Delannoy, J.J., 2012. 1.4 kyrs of flash flood events in the
1256 Southern European Alps: implications for extreme precipitation patterns and forcing
1257 over the north-western Mediterranean area 9097.
- 1258 Wilhelm, B., Ballesteros Canovas, J.A., Corella Aznar, J.P., Kämpf, L., Swierczynski, T., Stoffel,
1259 M., Støren, E., Toonen, W., 2018. Recent advances in paleoflood hydrology: From
1260 new archives to data compilation and analysis. *Water Security* 3, 1–8.
1261 <https://doi.org/10.1016/j.wasec.2018.07.001>
- 1262 Wilhelm, B., Rapuc, W., Amann, B., Anselmetti, F.S., Arnaud, F., Blanchet, J., Brauer, A.,
1263 Czymzik, M., Giguët-Covex, C., Gilli, A., Glur, L., Grosjean, M., Irmeler, R., Nicolle, M.,
1264 Sabatier, P., Swierczynski, T., Wirth, S.B., 2022. Impact of warmer climate periods on
1265 flood hazard in the European Alps. *Nat. Geosci.* 15, 118–123.
1266 <https://doi.org/10.1038/s41561-021-00878-y>
- 1267 Wilhelm, B., Sabatier, P., Arnaud, F., 2015. Is a regional flood signal reproducible from lake
1268 sediments? *Sedimentology* 62, 1103–1117. <https://doi.org/10.1111/sed.12180>
- 1269 Yemane, W., 2008. Challenges and Prospects of Commercial Agriculture Enterprise
1270 Development and the Afar Pastoralists: The Case of Tendaho Dam and Irrigation
1271 Project. Addis Ababa University, Addis Ababa.
- 1272 Zaroug, M.A.H., Eltahir, E.A.B., Giorgi, F., 2014. Droughts and floods over the upper
1273 catchment of the Blue Nile and their connections to the timing of El Niño and La Niña
1274 events. *Hydrol. Earth Syst. Sci.* 18, 1239–1249. [https://doi.org/10.5194/hess-18-](https://doi.org/10.5194/hess-18-1239-2014)
1275 [1239-2014](https://doi.org/10.5194/hess-18-1239-2014)
- 1276
- 1277

Mis en forme : Français (France)

Mis en forme : Italien (Italie)